High-resolution model simulation of the interannual and seasonal variability of the Weddell Gyre during 1958 - 2018

Julia Neme[1], Matthew H. England[2], and Andrew McC. Hogg[3]

[1]UNSW Australia
[2]University of New South Wales
[3]Australian National University

November 30, 2022

Abstract

The Weddell Gyre's variability on seasonal and interannual timescales is investigated using an ocean-sea ice model at three different horizontal resolutions. The model is evaluated against available observations to demonstrate that the highest resolution configuration (0.1° in the horizontal) best reproduces observed features of the region. The simulations suggest that the gyre is subject to large variability in its circulation that is not captured by summer-biased or short-term observations. The Weddell Gyre's seasonal cycle consists of a summer minimum and a winter maximum and accounts for changes that are between one third and a half of its mean transport . On interannual time scales we find that the gyre's strength is correlated with the local Antarctic easterlies and that extreme events of gyre circulation are associated with changes in sea ice concentration and the characteristics of warm inflow at the eastern boundary.

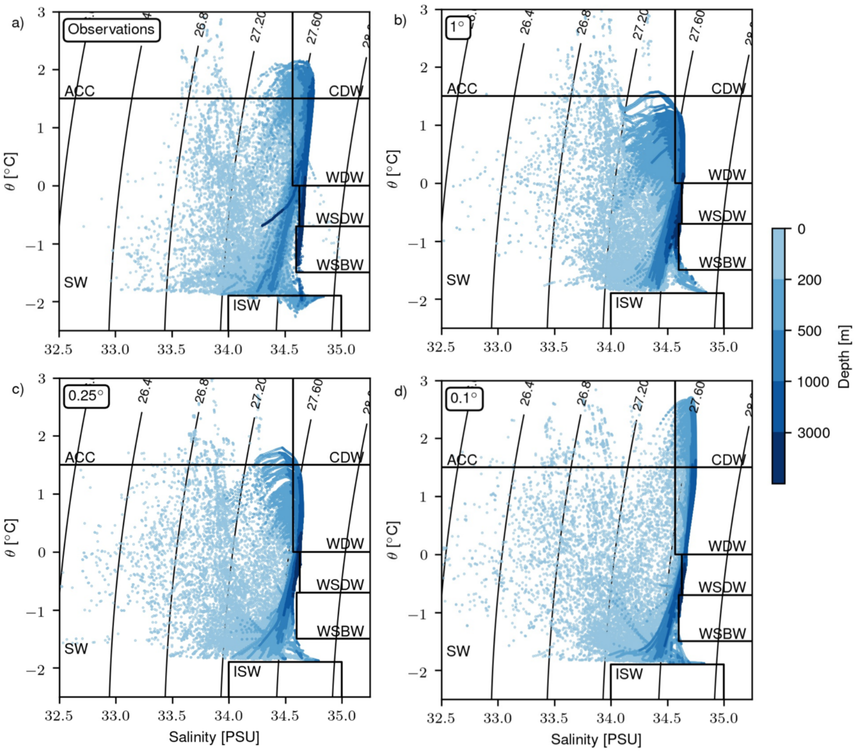
a)
Observations
b)
1°
c)
0.25°
d)
0.1°
ACC
CDW
WDW
WSDW
WSBW
SW
ISW
26.4
26.8
27.20
27.60
θ [°C]
Salinity [PSU]
Depth [m]
0
200
500
1000
3000

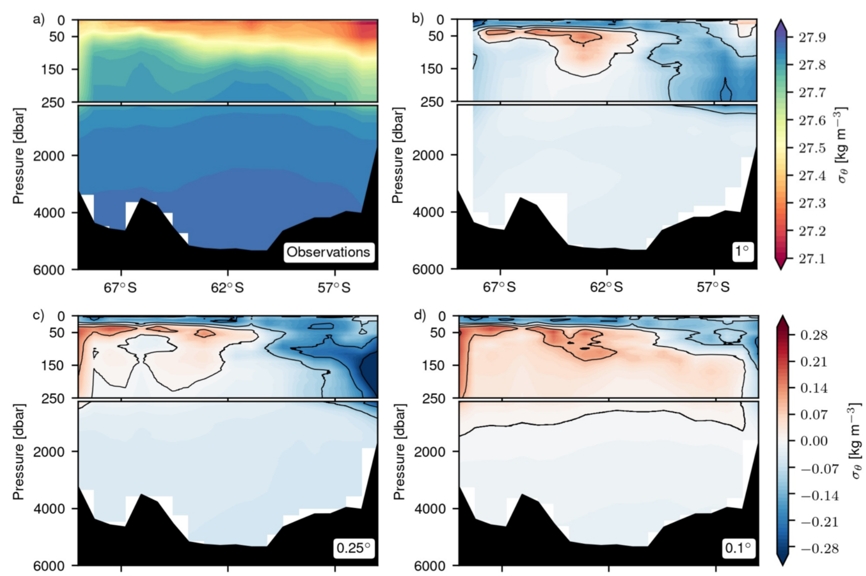
a)
b)
c)
d)
Observations
1°
0.25°
0.1°
Pressure [dbar]
67°S
62°S
57°S
σθ [kg m−3]
27.9
27.8
27.7
27.6
27.5
27.4
27.3
27.2
27.1
0.28
0.21
0.14
0.07
0.00
−0.07
−0.14
−0.21
−0.28

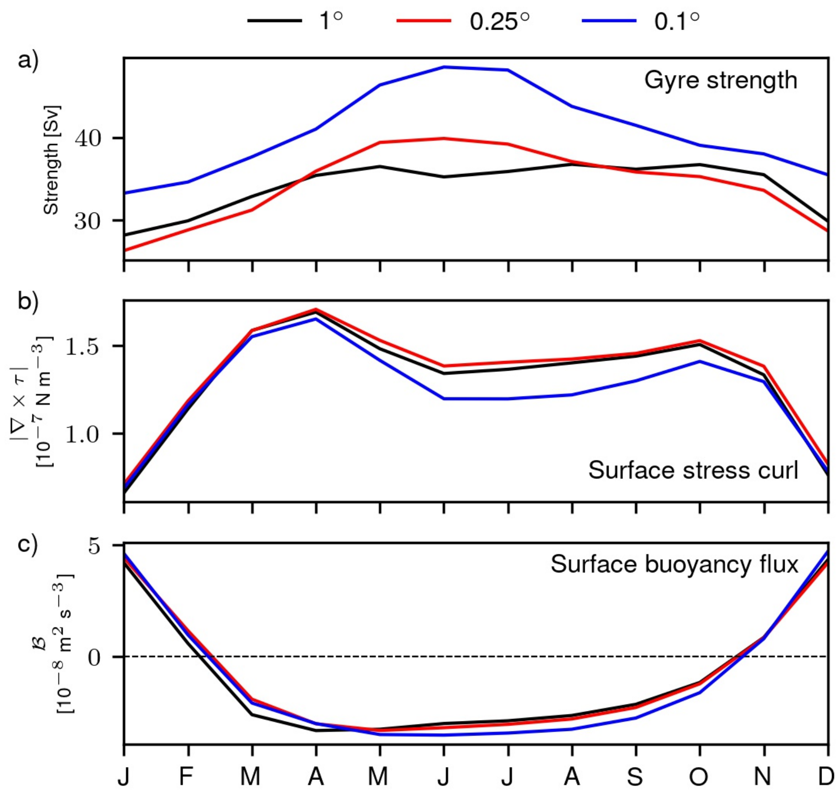
1°
0.25°
0.1°
a)
Gyre strength
Strength [Sv]
40
30
b)
$|\nabla \times \tau|$
$[10^{-7}$ N m$^{-3}]$
1.5
1.0
Surface stress curl
c)
Surface buoyancy flux
$\mathcal{B}$
$[10^{-8}$ m^2 s$^{-3}]$
5
0
J
F
M
A
M
J
J
A
S
O
N
D

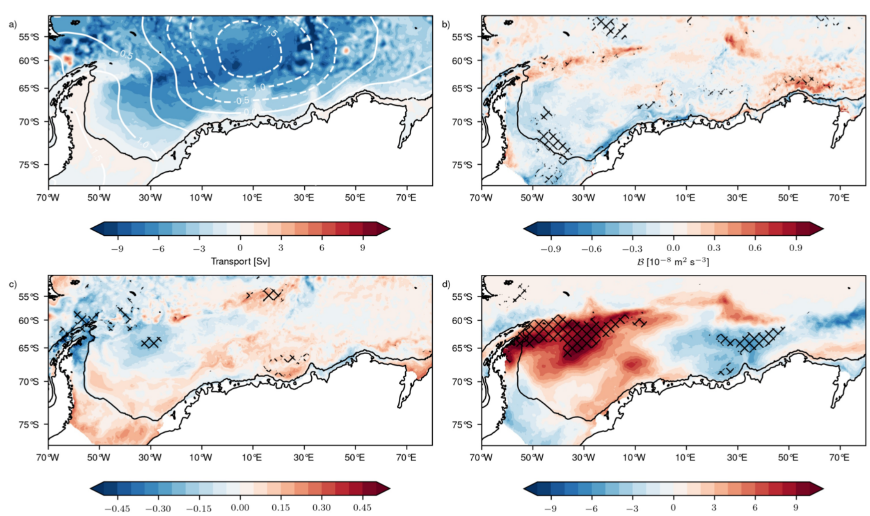
a)
b)
c)
d)
55°S
60°S
65°S
70°S
75°S
70°W
50°W
30°W
10°W
10°E
30°E
50°E
70°E
Transport [Sv]
$\mathcal{B}$ $[10^{-8}$ m^2 s$^{-3}]$
θ [°C]
Sea ice concentration [%]

High-resolution model simulation of the interannual and seasonal variability of the Weddell Gyre during 1958 - 2018

J. Neme[1,2], M. H. England[1,2], A. McC. Hogg[3]

[1]Climate Change Research Centre and ARC Centre of Excellence for Climate Extremes, University of New South Wales, Sydney, Australia.
[2]Australian Centre for Excellence in Antarctic Science, University of New South Wales, Sydney, Australia.
[3]Research School of Earth Science and ARC Centre of Excellence for Climate Extremes, Australian National University, Canberra, Australia.

Key Points:

- The Weddell Gyre, as simulated by a global coupled ocean-sea ice model, displays large variability on seasonal and interannual time scales.
- There is evidence of low frequency (decadal) variability in the Weddell Gyre's strength, but no significant trends during study period.
- Years of extreme strong/weak Weddell Gyre flow are shown to be linked to anomalous winds, ocean temperatures and sea ice concentration.

Corresponding author: Julia Neme, `j.neme@unsw.edu.au`

Abstract

The Weddell Gyre's variability on seasonal and interannual timescales is investigated using an ocean-sea ice model at three different horizontal resolutions. The model is evaluated against available observations to demonstrate that the highest resolution configuration (0.1° in the horizontal) best reproduces observed features of the region. The simulations suggest that the gyre is subject to large variability in its circulation that is not captured by summer-biased or short-term observations. The Weddell Gyre's seasonal cycle consists of a summer minimum and a winter maximum and accounts for changes that are between one third and a half of its mean transport . On interannual time scales we find that the gyre's strength is correlated with the local Antarctic easterlies and that extreme events of gyre circulation are associated with changes in sea ice concentration and the characteristics of warm inflow at the eastern boundary.

Plain Language Summary

The Weddell Gyre, located east of the Antarctic Peninsula, is one of the largest features of the ocean circulation of the Southern Hemisphere. It is adjacent to an important site of bottom water formation, a process that sequesters carbon and heat from the atmosphere and sets the density of the deep ocean, therefore making the region important for global climate. However, extensive sea ice cover throughout the year has historically prevented continuous observations. Several unique features of the gyre, such as open boundaries and intense surface buoyancy fluxes, make the identification of its forcing mechanisms difficult. A deeper understanding of the dynamics in this remote region will shed light on the role of the gyre in our present climate, and help us understand its potential evolution with climate change. We use a high resolution numerical model which shows that the Weddell Gyre undergoes large seasonal and interannual changes. We find that the gyre spins up during winter and slows down during summer, and that strong/weak events in our model simulation are correlated with the strength of the regional easterly winds close to the Antarctic continent. These strong/weak events affect sea ice cover, water mass characteristics and bottom water production.

1 Introduction

The lateral circulation in the Weddell Sea is dominated by the Weddell Gyre, one of the largest features of the ocean circulation south of the Antarctic Circumpolar Current (ACC). The Weddell Gyre is characterized by a broad cyclonic circulation spanning from the Antarctic Peninsula until approximately 30°E (Deacon, 1979), schematized in Figure 1. The gyre is one of the southernmost open ocean reaches in the world, with several features that make it an intriguing and relevant component of the Southern Ocean circulation. A strong interaction between ocean and sea ice favours large surface buoyancy fluxes that, in combination with a weak stratification, create a connection between the atmosphere, the ocean surface and the ocean bottom. For example, located in the southwestern Weddell Sea is one of the major formation sites of Antarctic Bottom Water (AABW) (Meredith, 2013), a process which supports the deepest limb of the global overturning circulation and involves waters that are circulated and transformed within the gyre. Despite the Weddell Gyre's relevance to global climate, the extensive sea ice cover throughout most part of the year has historically hampered long-term, continuous observational efforts and the present knowledge of the gyre's circulation and variability is mostly limited to the summer months.

The Weddell Gyre's circulation has been traditionally associated with the negative stress curl given by a large scale surface wind field consisting of westerlies to the north, a circumpolar band of easterly winds surrounding Antarctica and a low pressure system embedded at around 30°E, 65°S (Gordon et al., 1981; Deacon, 1979). The surface wind pattern makes the center of the gyre a region of divergence of Ekman transport, characterized by a depression of sea level (Armitage et al., 2018), wind driven Ekman upwelling and a doming of subsurface isopycnals (Klatt et al., 2005; Schröder & Fahrbach, 1999). The Antarctic continent to the south and west, together with a series of submarine ridges to the north provide a clear topographic barrier to the flow. There is no such barrier on the eastern boundary of the gyre, which has been suggested to be a dynamic feature located between 30°E and 70°E. It is at this boundary where relatively warm and saline Circumpolar Deep Water (CDW) enters the gyre, partly following an advective and partly following an eddy-driven pathway (Ryan et al., 2016; Cisewski et al., 2011; Leach et al., 2011; Schröder & Fahrbach, 1999), hereafter called Warm Deep Water (WDW). The properties of WDW that enter the gyre are modified along its westward path by mixing and upwelling until some of this modified Warm Deep Water (mWDW) crosses the shelf break at the southern Weddell Sea, where it mixes with High Salinity Shelf Water (HSSW), formed by cooling and brine rejection, to produce Weddell Sea Deep Water (WSDW). Some of this WSDW is able to escape the gyre towards the Scotia Sea and becomes AABW (R. A. Locarnini et al., 1993).

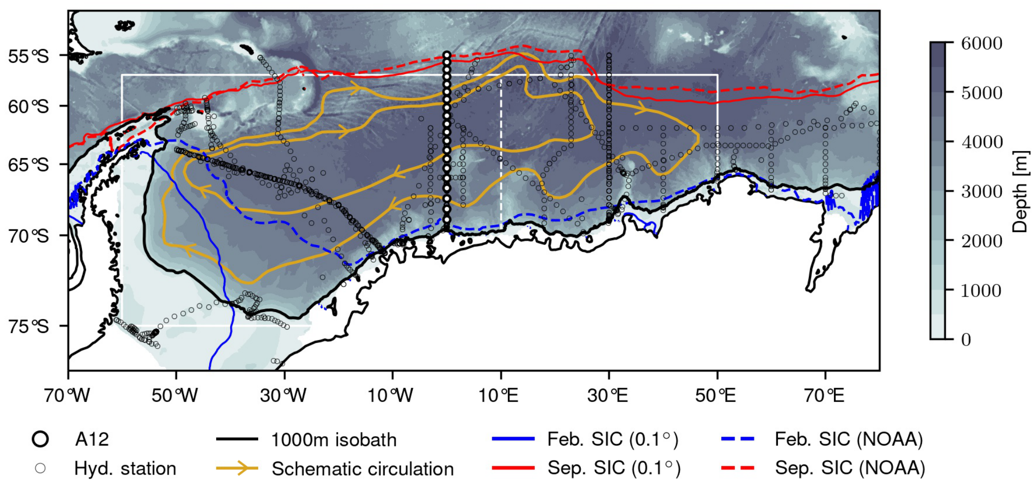

Figure 1. Bathymetry of the Weddell Sea with the 1000m isobath (black contour) and February (blue) and September (red) sea ice extent defined by 15% sea ice concentration from ACCESS-OM2-01 (solid line) and NOAA/NSIDC Climate Data Record of Passive Microwave Sea Ice Concentration, Version 3 (dashed line). The arrows show a schematic of the Weddell Gyre circulation and the white solid box marks the area within which surface stress and buoyancy fluxes are averaged to build a time series in Figures 8 and 10. The Weddell Gyre strength is calculated west of the dashed orange line at 10°E.

Observational and modelling studies have estimated the Weddell Gyre strength to be between 30 and 100 Sv, a wide range of values that reflect the strong dependence of gyre strength on the methodology used. Hydrography-based estimates may underestimate gyre strength because they are biased towards summer conditions, thus excluding a possible winter intensification. Furthermore, the weak stratification that characterizes the region means that the assumption of a level of no motion, required to derive transports from the thermal wind equations, may not be appropriate (Cisewski et al., 2011; Park & Gambéroni, 1995; Fahrbach et al., 1991). Numerical models are not subject to such experimental difficulties but their evaluation is limited by the scarcity of observations in the region. The gyre exhibits a persistent double-cell circulation structure whose origin remains unclear, but further contributes to the uncertainties in gyre transport (Reeve et al., 2019; Mazloff et al., 2010; Wang & Meredith, 2008; Beckmann et al., 1999; Orsi et al., 1990).

The present knowledge of the variability of the Weddell Gyre, its magnitude, drivers and time scales is greatly limited by the lack of continuous observations. Repeat hydrographic sections have been used to determine that the properties of the Weddell Gyre's water masses display significant variations associated with the gyre's circulation (Fahrbach et al., 2011; Behrendt et al., 2011; Fahrbach et al., 2004). For example, changes in the properties of AABW exported from the Weddell Sea have been linked to wind-forced changes in the gyre's baroclinic structure (Jullion et al., 2010; Meredith et al., 2011, 2008). The northern and southern limbs of the gyre have been suggested to vary independently and not necessarily in phase, responding to different forcing mechanisms (Fahrbach et al., 2011). The northern boundary could be driven by the westerly winds, while the southern limb of the gyre, comprised of a westward flowing current system referred to as the Antarctic Slope Current (ASC), partly forced by the easterly winds close to the Antarctic continent. Easterlies force an Ekman transport towards the coast, raising sea level and driving a geostrophic flow that displays significant variability on seasonal and interannual time scales (A. Naveira Garabato et al., 2019; Armitage et al., 2018; Mathiot et al., 2011). Interannual variability in gyre strength has also been related to climate modes, such as the Southern Annular Mode (SAM) or El Nio oscillation (Armitage et al., 2018; Martinson & Iannuzzi, 2003). Few studies take into consideration the influence of sea ice and surface buoyancy fluxes as possible driving mechanisms, despite their relevance to the dynamics of the region.

This study analyzes numerical simulations derived from a coupled numerical model (described in Section 2.1) configured over three different horizontal resolutions (1°, 0.25° and 0.1°) to study the Weddell Gyre's variability on seasonal to interannual timescales, and its connection to possible forcing mechanisms including wind stress and buoyancy fluxes. In Section 3 the model is evaluated against available observations to assess its strengths and weaknesses in the study region. For this evaluation we use the Armitage et al. (2018) dynamic ocean topography product and temperature and salinity profiles from available hydrographic stations in the region. Section 4 characterizes the Weddell Gyre mean state in model simulations and Section 5 and 6 the gyre's variability on seasonal and interannual timescales respectively. Section 7 summarizes the results and discusses their relevance for our current knowledge of the Weddell Gyre circulation.

1.1 Ocean/Sea Ice Model

This study uses the Australian Community Climate and Earth System Simulator (ACCESS-OM2) (Kiss et al., 2020), a global ocean-sea ice model. This model is available at three different horizontal resolutions, namely 1° and 0.25° with 50 vertical levels and 0.1° with 75 vertical levels. The ocean component of the model is the Modular Ocean Model (MOM) version 5.1, developed by the Geophysical Fluid Dynamics Laboratory (`https://mom-ocean.github.io/`) and the sea ice component is the Los Alamos sea ice model (CICE) version 5.1.2 from Los Alamos National Laboratories (`https://github.com/CICE-Consortium/CICE-svn-trunk/tree/cice-5.1.2`). All three configurations are initialized from a rest state with zero sea level, temperature and salinity given by the World Ocean Atlas 2013 v2 0.25° decav product (M. Locarnini et al., 2018; Zweng et al., 2019) and are forced by a prescribed atmosphere from JRA55-do reanalysis v1.4 for the period 1958 to 2018 (Tsujino et al., 2018). The model is continuously cycled through this 61-year period, from which we select the third forcing cycle since it is the latest cycle available for all three resolutions. The three model configurations are consistent with each other which allows to infer the importance of resolution in the study region. There is a general improvement at the highest 0.1° configuration when solving several features of the ocean: those relevant for this study are the representation Southern Ocean water masses, the overturning circulation and the characteristics of the circulation on the Antarctic continental shelf (Kiss et al., 2020; Moorman et al., 2020; Morrison et al., 2020).

1.2 Satellite Observations

We evaluate ACCESS-OM2 in the Weddell Gyre region against the dynamic topography of the satellite product developed by Armitage et al. (2018), a unique data set in the Southern Ocean where extensive sea ice cover has historically hampered long term continuous observations using traditional radar altimetry. The product consists of monthly composites of dynamic ocean topography spanning a five year period (2011 to 2016) at 50km horizontal resolution, referenced to the GOCO05c combined gravity field model (Fecher et al., 2017). A limitation of this satellite product is the dependence of its mean dynamic topography on the geoid model, which has larger errors and uncertainties toward the Antarctic continent due to the sparsity of the data being assimilated. These uncertainties do not affect sea level anomalies, i.e. observed variability, because the geoid is time invariant. The product also displays some north-south striping artifacts generated by the satellite's orbital precession (see Fig. 5 of Armitage et al. (2018)). To compare ACCESS-OM2 sea level with satellite observations, we interpolated the model to the satellite product's grid and applied an offset to remove the spatially uniform footprint of geoid uncertainties in the satellite product. The offset is defined as the average difference between the mean sea level fields of each model simulation and observations for the entire region covered by the satellite product.

1.3 Hydrographic Data

The model's temperature and salinity is evaluated against hydrographic observations in the Weddell Gyre region downloaded from the Clivar and Carbon Hydrographic Data Office (CCHDO). We selected all publicly available CTD profiles in the region, a total number of 1576. Table 1 has information on the hydrographic cruises and their locations are shown in Figure 1. To compare against ACCESS-OM2, we select the nearest grid point and corresponding monthly composite within the model output and we interpolate it to the same vertical levels. With this approach we obtain synthetic profiles within the ACCESS-OM2 model simulations to evaluate the temperature-salinity structure of the gyre. To give further insight into the gyres vertical structure, we selected one of the most repeated WOCE transects in the region, A12 nominally at the Greenwich Meridian (see Figure 1), to calculate an average potential density cross-section. Analogous to the procedure for individual hydrographic stations, we select the monthly composites of model data that correspond to the repeat A12 cruises, interpolate the vertical level, and then calculate the anomalies of the model with respect to the observations.

1.4 Barotropic streamfunction definition

The barotropic streamfunction, ψ, is used to study the gyre's transport and is defined as the meridional integral of the depth-integrated zonal mass transport M_x:

$$\psi(x, y) = \int_{y_0}^{y} \frac{M_x(x, y')}{\rho(y - y_0)} dy' \qquad (1)$$

where we take ρ as an average density of 1035 $kg\ m^{-3}$ and the integration goes from south to north starting at the Antarctic continent (y_0). By this defintion, ψ takes negative values for the cyclonic circulation of the Weddell Gyre. The gyre strength (GS) is derived from ψ by calculating its minimum in the region bounded by the white box in Figure 1 west of 10°E (dashed white line) and taking the absolute value:

Table 1. Summary of the hydrographic cruises used to evaluate the model. Cruise locations are indicated in Figure 1. The expocode is the identifier for the data sets archived at the Carbon and Climate Hydrographic Data Office (CCHDO; `http://cchdo.ucsd.edu`).

Expocode	Line	Start date	End date	Principal Investigator
06AQANTVIII_2	SR02, SR04	1989-09	1989-10	Eberhard Fahrbach
06AQANTIX_2	SR04	1990-11	1990-12	Eberhard Fahrbach
06AQANTX_4	A12, SR04	1992-05	1992-08	Peter Lemke
35MFCIVA_1	I06S	1993-01	1993-03	Alain Poisson
74DI200_1	S04	1993-02	1993-03	Robert R. Dickson
74JC10_1	A23	1995-03	1995-05	Karen J. Heywood and Brian A. King
320696_3	S04, S04I	1996-03	1996-04	Thomas Whitworth
35MF103_1	I06S	1996-02	1996-03	Alain Poisson
06AQANTXIII_4	S04A, SR04	1996-03	1996-05	Eberhard Fahrbach
06AQANTXV_4	SR04	1998-03	1998-05	Eberhard Fahrbach
06AQ199901_2	A12	1999-01	1999-03	Eberhard Fahrbach
06AQ200012_3	A12	2000-12	2001-01	Eberhard Fahrbach
06AQ200211_2	A12	2002-11	2003-01	D.K. Ftterer
06AQ20050102	A12	2005-01	2005-04	Eberhard Fahrbach
09AR20060102	S04I	2006-01	2006-03	Mark Rosenberg
06AQ20071128	A12	2007-11	2008-02	Ulrich Bathmann
33RR20080204	I06S	2008-02	2008-03	Kevin Speer
06AQ20080210	A12	2008-02	2008-04	Eberhard Fahrbach
06AQ20101128	A12	2010-11	2011-02	Eberhard Fahrbach
06AQ20141202	PS89	2014-12	2015-02	Olaf Boebel

$$GS = |\, min\{\psi\} \,| \tag{2}$$

The gyre strength definition is limited to 10°E to exclude the unstable, eddy-rich flow of the eastern region, but nonetheless encompasses the main structure of the mean gyre (see Section 3.2). The barotropic streamfunction is also used to define the boundary of the Weddell Gyre as the 12 Sv contour with the purpose of tracking changes in the gyre's area over time.

1.5 Surface stress and buoyancy fluxes

To assess the role of stress over the ocean's surface as a possible driver of the circulation, we calculate the total surface stress from model output taking into account the relative contributions of air/ocean and ice/ocean stresses ($\tau_{air/ocean}$ and $\tau_{ice/ocean}$ respectively) weighted by sea ice concentration. The curl of the total surface stress, $\nabla\times\tau$, is defined as:

$$\nabla\times\tau = \nabla\times((1-\alpha_{ice})\tau_{air/ocean}) + \nabla\times(\alpha_{ice}\tau_{ice/ocean}) \tag{3}$$

where α_{ice} is sea ice concentration. To build a time series, $\nabla\times\tau$ is averaged in the region bounded by the white box in Figure 1 excluding grid cells in which the bathymetry is shallower than 1000m. We show the absolute value of the surface stress curl so that stronger curl anomalies are represented by positive values.

Surface buoyancy fluxes are also considered as a possible driver of the gyre's variability, taking into account contributions due to both heat and freshwater exchanges. The surface buoyancy flux is defined as:

$$\mathcal{B} = \frac{g\alpha Q}{c_w \rho} + g\beta F_w s \tag{4}$$

where ρ is surface density, g is the acceleration due to gravity, c_w the specific heat of sea water, α the thermal expansion coefficient, β the saline contraction coefficient, s surface salinity and Q and F_w are the heat and freshwater fluxes, positive representing a buoyancy gain by the ocean. The Python implementation of the Gibbs Sea Water Oceanographic Toolbox of TEOS-10 (`https://teos-10.github.io/GSW-Python/`) was used to compute the quantities derived from temperature and salinity. The largest buoyancy fluxes in the Weddell Sea region are found over the continental shelf, so $\mathcal{B}$ is averaged at depths shallower than 1000m to build a time series.

1.6 Climate indices

We use the Southern Annular Mode (SAM) index as a proxy for the meridional expansion/contraction of the band of westerlies surrounding the Antarctica to evaluate the connection between the gyre and large-scale atmospheric modes of variability. This index is calculated as the difference between the zonal anomalies of sea level pressure at 40°S and 65°S, (Marshall, 2003), from the JRA55 reanalysis, the atmospheric data set used to force the model. To verify that local changes in the westerlies are not significantly different from the circumpolar average we re-evaluate the SAM index in a limited domain, calculating the zonal anomalies with respect to the mean of the Weddell Sea and find no significant differences. By analogy we define a different index to track the intensification/weakening of the local easterly winds, hereafter denoted EAS, defined as the difference in the zonal anomalies of sea level pressure at 65°S and 72°S. Contrary to the SAM index, since the easterlies display a large zonal variation, the EAS is calculated between 30°W and 70°E with the intention of focusing only on regional changes.

1.7 Analysis period

Long term climatological fields are calculated for the period 1958 to 2018 for ψ, $\nabla\times\tau$ and $\mathcal{B}$, from which we calculate the annual cycles of gyre strength, surface stress curl and buoyancy fluxes as described in the previous sections. To study interannual variability, these metrics together with the SAM and EAS indices are calculated using monthly composite fields for the full 61-year period, and subsequently the annual cycle is removed to obtain anomalies. We also apply a 12-month running mean to filter out high frequency variability. The 0.1° experiment is used to define strong and weak events of Weddell Gyre flow as periods longer than 6 months during which gyre strength is beyond $\pm 0.8SD$ of the gyre strength time series smoothed with a 10-year running mean. Once the events are identified we composite the streamfunction, sea level pressure, surface buoyancy fluxes, subsurface temperature maximum and sea ice concentration anomaly fields to characterise the differences between anomalously strong and weak gyre periods and the impact on the region. Additionally, we calculate the linear correlation coefficients between the gyre strength time series and the anomaly fields of surface buoyancy fluxes, subsurface temperature maximum and sea ice concentration in order to identify regions where they are significantly correlated to, and thus likely affected by, gyre strength.

2 Model Evaluation

Satellite observations (Armitage et al., 2018) show the Weddell Gyre as an elongated depression of sea level, indicative of a cyclonic geostrophic current, with its main axis oriented in the northeast-southwest direction (Figure 2a). Figures 2b, c and d show the difference between the model and satellite observed mean dynamic topography for the 1°, 0.25° and 0.1° configurations respectively. If this difference were spatially constant, then the derived surface geostrophic circulation would be the same since the velocity in between two grid points is proportional to the difference in elevation between those two points. The 0.1° simulation exhibits the smallest horizontal gradients in the sea level difference with observations (Figure 2d), not only within the gyre's boundary, but also in the southwestern continental shelf, the eastern region and within the ACC, which indicates that the highest resolution configuration better represents the observed Weddell Gyre geostrophic flow.

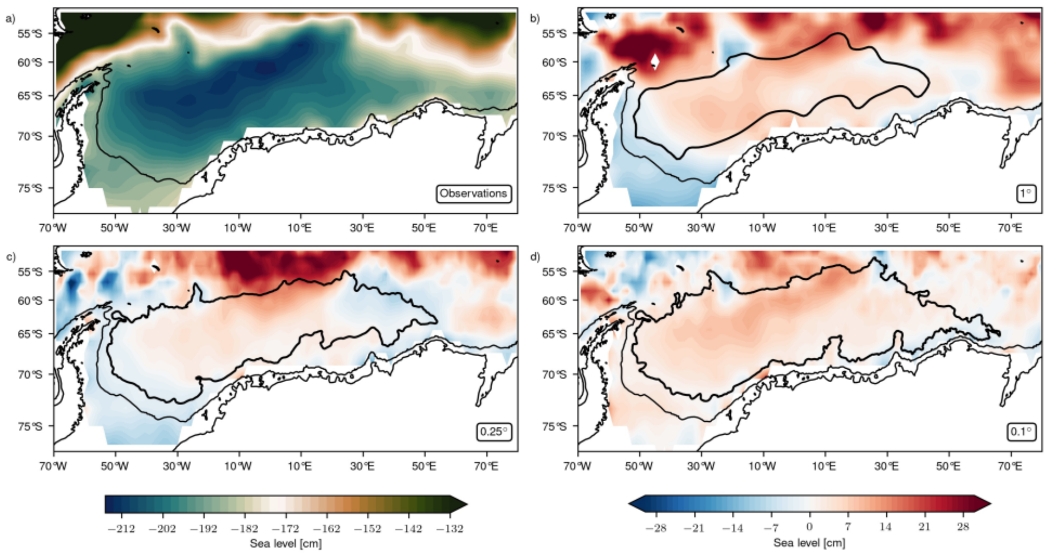

Figure 2. (a) Mean sea level from satellite observations for the period 2011 to 2016 (Armitage et al., 2018). Model's mean sea level for the same period minus satellite observations for the (b) 1°, (c) 0.25° and (d) 0.1° resolution configurations, with gyre's mean boundary (defined as the 12 Sv barotropic streamfunction contour) in thick black. Thin black contour in all panels marks the 1000m isobath.

The Armitage et al. (2018) data set can also be used to compare variability. We compute the correlation coefficient between the satellite and model sea level at every grid point for the period 2011 to 2016 and use them to build correlation maps, shown in Figures 3a, b and c with significant correlations hatched. A north-south striping pattern is visible in the correlation coefficients that reflects an artifact from the satellite's orbit. Taking this artifact into consideration, we infer that within the gyre, model and observations are significantly correlated, with no large differences between model configurations. However, the correspondence between model and observations breaks down within the ACC, which we attribute to the presence of eddies that the model is not expected to reproduce at the precise location and time as they appear in observations. Unlike the comparison between model and observations within the gyre, in the southwestern continental shelf the ability of the model to reproduce observed variability improves significantly with resolution, with higher, significant correlations for the 0.1° configuration. However, the correlation maps do not fully illustrate differences in the model's variability with respect to observations, which is why we calculate the root mean square error (RMSE) within the gyre over the observational record, Figure 3d. We observe that the RMSE within the Weddell Gyre is in phase between model configurations and of similar magnitude, indicating that the departure from observations is consistent across resolution and therefore likely due to errors in model forcing compared to observations. There is also no seasonality in the error (e.g. the error is not consistently larger in winter), which further suggests that the error is due to biases in the model's forcing rather than biases in satellite observations associated with sea ice cover.

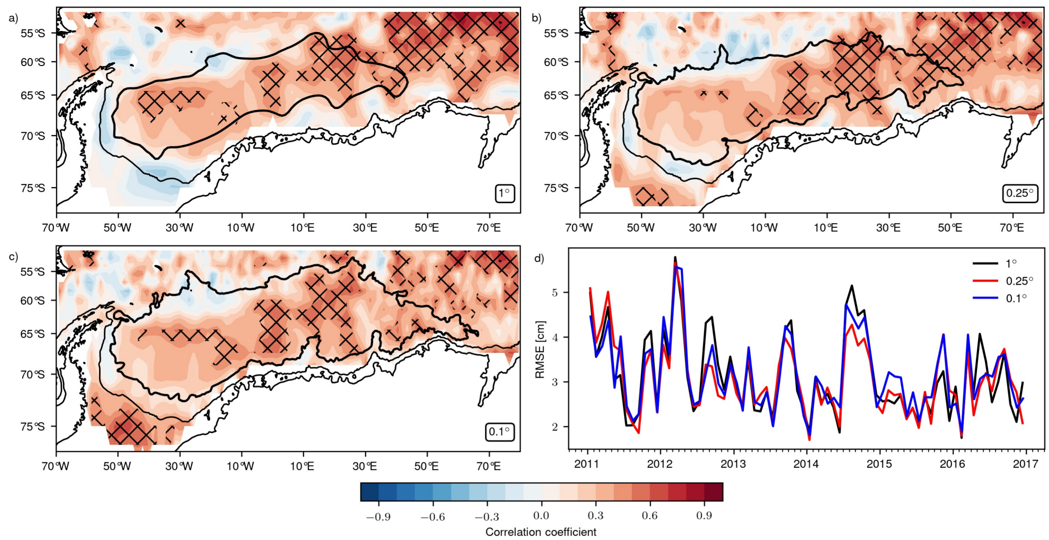

Figure 3. Correlation coefficients with satellite observations for models at (a) 1°, (b) 0.25° and (c) 0.1° resolution with hatching for significant correlations ($p < 0.05$). Mean gyre's boundary in thick black contour and 1000m isobath in thin black contour. (d) RMSE between model and observations calculated for a region encompassing the gyre [30°W, 30°E]x[70°S, 60°S].

Apart from evaluating the model's sea level, we can evaluate the model's temperature and salinity structure against observations. Figure 4 shows modeled and observed temperature-salinity diagrams comparing all available hydrographic stations in the Weddell Gyre region at locations indicated in Figure 1. It is possible to identify different water masses in observations (Figure 4a) according to their potential temperature and salinity: namely warm and saline CDW, colder WDW and a distinct tail of colder Weddell Sea Deep and Bottom Waters (WSDW and WSBW respectively). There are also some stations on the continental shelf that indicate the presence of Ice Shelf Water (ISW) with temperatures lower than the surface freezing point (-1.9° C). The ability of the model to reproduce the distinct characteristics of these water masses is highly dependent on resolution. The coarser 1° resolution does not show the presence of CDW in the region, has a colder, fresher than observed WDW and the characteristics of its bottom waters are less distinct from shallower waters than observed. There is a slight improvement in the 0.25° configuration which shows a trace of CDW and a better reproduction of WDW characteristics. The improvement is clearest for the 0.1° resolution configuration which captures the presence of CDW in the region, although warmer than observed, as well as achieving a better representation of WDW than the two coarser resolutions. The 0.1° simulation also shows some trace of the bottom waters, albeit less distinct than observed, which could be related to the coarse vertical resolution of the model relative to the station observations (50 levels for the 1° and 0.25° and 75 levels for the 0.1° configuration). Moreover, none of the model configurations capture the presence of supercold ISW because the model lacks the ice shelf cavities where this water mass is formed. Since ISW participates in deep and bottom water production, the model's misrepresentation of these dense waters could be related to its inability to generate ISW.

The average cross section of potential density at the Greenwich Meridian, Figure 5, shows the doming of isopycnals that characterizes the center of the gyre and the in-

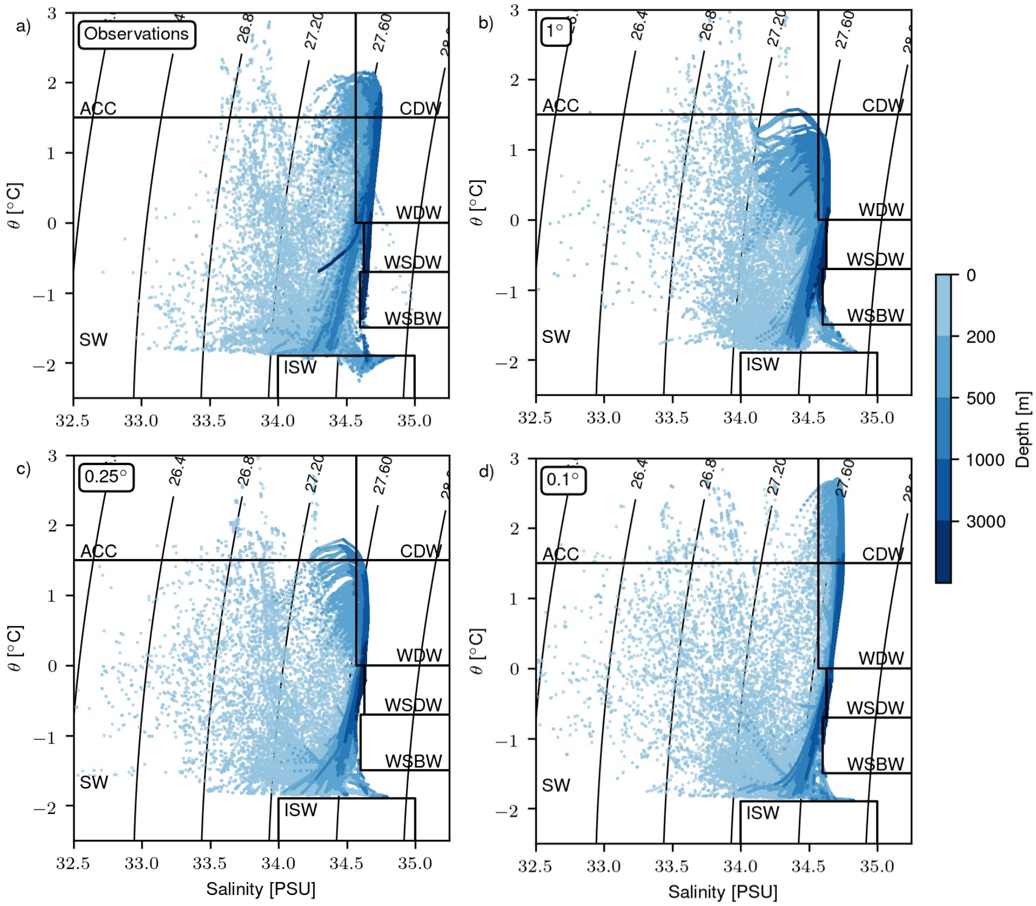

Figure 4. Temperature-salinity diagrams for all stations in Figure 1 for (a) hydrographic observations and for model runs at (b) 1°, (c) 0.25° and (d) 0.1° resolution, color coded by their depth. Antarctic Circumpolar Current = ACC, Circumpolar Deep Water = CDW, Warm Deep Water = WDW, Weddell Sea Deep Water = WSDW, Weddell Sea Bottom Water = WSBW, Surface Water = SW, Ice Shelf Water = ISW.

fluence of Maud Rise, north of 67°S, on top of which sits a cold, fresh Taylor column. At around 58°S the sloping of the isopycnals shows the front that marks the transition from Weddell Gyre to the ACC. The differences between model and observations (Figures 5b, c and d) show that the largest discrepancies are located in the upper 250m of the water column. The most striking difference is the clear contrast between Weddell Gyre waters (denser than observed) and ACC waters (lighter than observed) for the 1° and 0.25° configurations, which means that for these resolutions the oceanic front at the northern boundary of the gyre is steeper than observed. This Weddell Gyre/ACC contrast is not apparent in the 0.1° resolution. On the other hand, all three configurations show anomalies of alternate sign within the gyre in a thin surface layer shallower than 50m and the underlying subsurface layers. Since the cross sections are representative of summer conditions, there is a shallow layer of light waters associated with sea ice melt that sits on top of the Winter Water (WW), so-called because it surfaces during winter when there is a weakening of the summer pycnocline associated with ice production. The model cross sections show for all resolutions a lighter than observed summer surface layer and a denser than observed winter subsurface layer, which means that the stratification is larger than observed in the model during the summer months. Below the upper 250m, the 0.1° configuration exhibits an improved representation of the observed potential density relative to the 1° and 0.25° simulations.

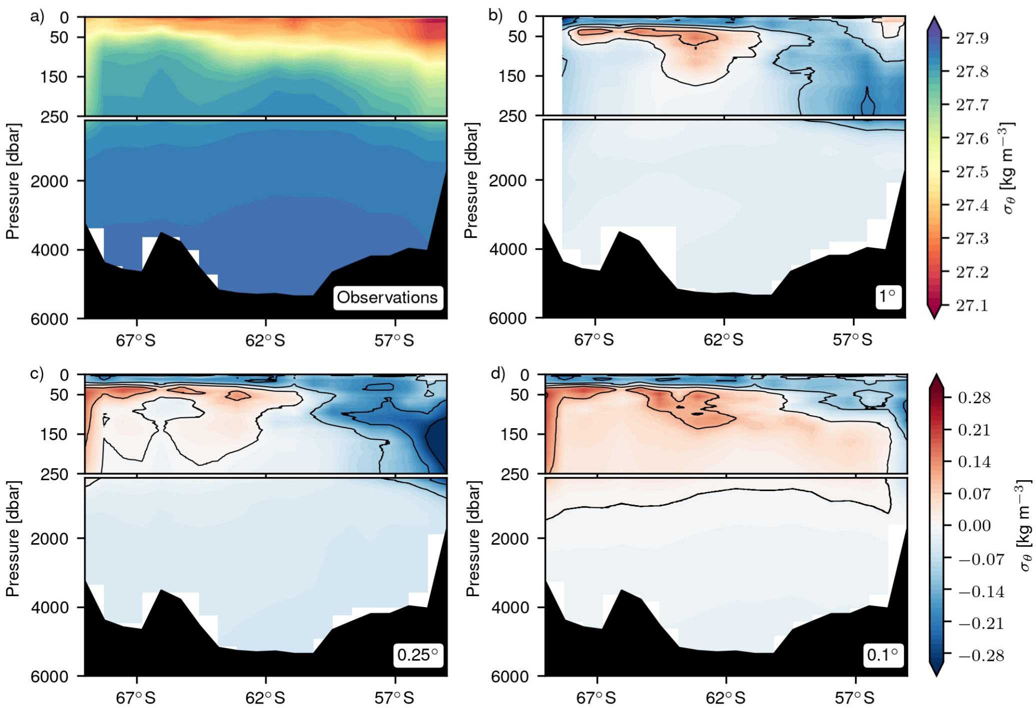

Figure 5. Average potential density (kg m^{-3}) section for A12 transect shown in Figure 1 for (a) hydrographic observations and the difference with observations for (b) 1°, (c) 0.25° and (d) 0.1° resolutions with 0.1 kg m^{-3} spacing between contours in black.

3 Weddell Gyre Mean State

The mean barotropic streamfunction for the entire 61 year period of the model run (1958 to 2018) in Figures 6a, c, e, shows an elongated cyclonic gyre with mean strengths of 34, 33 and 41 Sv and a seasonal range of 9, 14 and 15 Sv for the 1°, 0.25° and 0.1° resolutions respectively. The magnitude and spatial pattern of the Weddell Gyre as depicted by the model is in agreement with both observational and past modeling studies. All resolutions display a double lobed circulation structure, with a larger western cell and a recirculation close to the Greenwich Meridian. As the resolution increases, the region east of approximately 10°E becomes increasingly unstable and the cyclonic circulation expands towards the east along the coastline.

The barotropic circulation generally follows potential vorticity contours (approximated by f/H) at the south, west and northern boundaries; these contours are largely controlled by topographic features, indicating that the motion is steered by bathymetry. The larger spacing between f/H contours in the southern limb is associated with a broad, slow circulation that contrasts with a more intense northern boundary flow. At the northeastern boundary the flow crosses potential vorticity contours, where there is an abrupt deflection of f/H contours owing to a gap in the Southwestern Indian Ridge at around 30°E, 55°S. The crossing of f/H contours indicates that the flow experiences changes in its potential vorticity due to its interaction with topography, an interaction that is

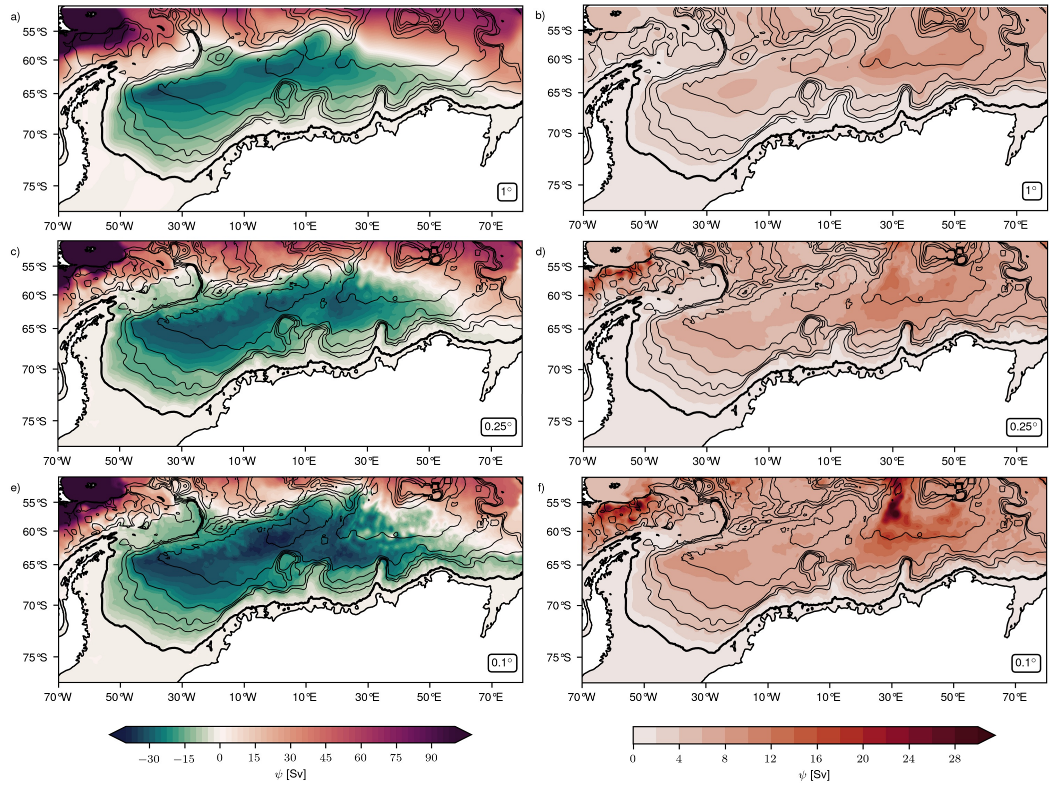

Figure 6. Mean barotropic streamfunction (Sv, 1 Sv = $10^6 m^3/sec$) for the period 1958 - 2018 for (a) 1°, (c) 0.25° and (e) 0.1° and its standard deviation for the (b) 1°, (d) 0.25° and (f) 0.1° resolution models with contours of potential vorticity (f/H) and 1000m isobath indicated by the thin and thick black contours respectively.

highly dependent on resolution. The deflection of f/H contours, together with the strong flow of the ACC, give rise to instabilities at the tail of the ridge particularly at 0.1° resolution, that leave a trace in the mean circulation (Figure 6e), as highlighted by the large values in the standard deviation of ψ (Figure 6f).

The subsurface temperature maximum can be used to trace the path CDW takes after entering the gyre at its eastern boundary. Observations show this warm inflow and the subsequent lowering of its temperature due to mixing as CDW flows to the west (see Figure 7a using Reeve et al. (2019) gridded data set as an example). The 0.1° simulation is the only configuration that displays such warm inflow. The improved accuracy of the 0.1° model in reproducing this feature of the gyre could be crucial, since the inflow affects the characteristics of bottom waters formed at the continental shelf (Couldrey et al., 2013; Jullion et al., 2014; Fahrbach et al., 2011).

4 Weddell Gyre Seasonal Cycle

The three model simulations show a seasonal cycle of gyre strength consisting of a winter intensification and a summer weakening (Figure 8a) that increases in amplitude with resolution and accounts for 36%, 46% and 44% of the variability in gyre strength for the 1°, 0.25° and 0.1° configurations respectively. There is a clear increase in transport from the 1° and 0.25° resolutions to the 0.1° resolution. The seasonal cycle of surface stress curl is strongly modulated by changes in sea ice concentration (α_{ice} in Equa-

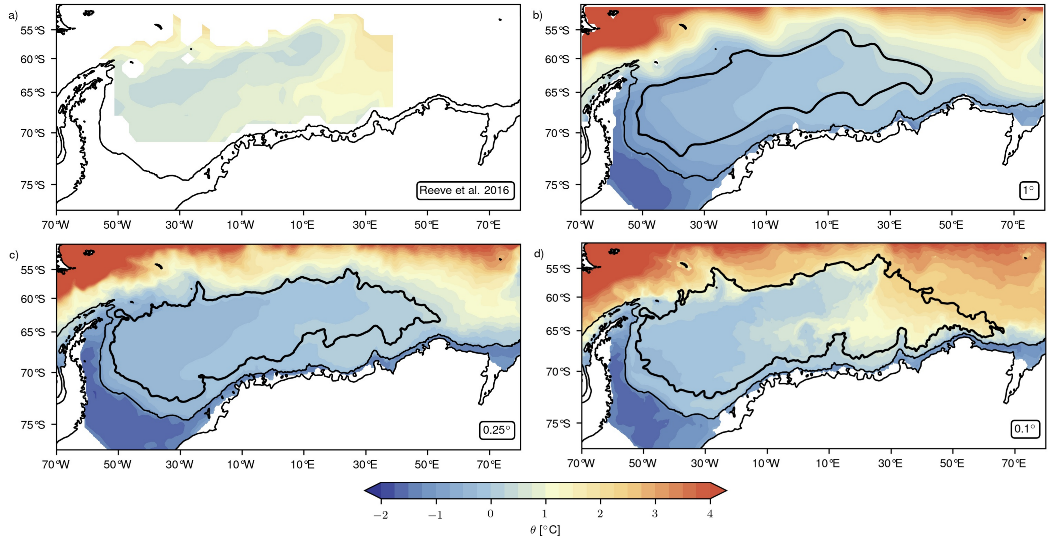

Figure 7. Subsurface mean potential temperature maximum for the period 2001 to 2014 from (a) the Reeve et al. (2016) product and for the period 1958 - 2018 from the (b) 1°, (c) 0.25° and (d) 0.1° resolution simulations. The thick black contour marks the gyre's boundary and the thin black contour the 1000m isobath.

tion 3): during the summer months, the minimum in sea ice concentration makes wind stress the primary contributor to the total stress curl. As the ice pack begins to develop, it damps the transfer of momentum from the atmosphere to the ocean, generating a winter minimum in total stress curl relative to the autumn peak. After reaching its maximum during August-September, α_{ice} begins to decrease, allowing for a second maximum in total stress curl during spring. The seasonal cycle of surface buoyancy fluxes, Figure 8c, is also strongly modulated by the presence of sea ice. During the summer, months sea ice melt, along with warmer air temperatures, result in a net surface buoyancy gain, with the opposite occurring during winter via sea-ice formation, brine rejection, and atmospheric cooling.

Correlations between gyre strength, surface stress curl and surface buoyancy fluxes are shown in Table 2. Gyre strength is significantly correlated with both forcing mechanisms considered, indicating that buoyancy losses and surface stress curl intensification are concurrent with a stronger gyre, with the exception of the 0.1° resolution simulation whose annual cycle of gyre strength is not correlated with the semi-annual cycle of surface stress curl. There is a clear increase in transport from the 1° and 0.25° simulations to the 0.1° that is not explained by differences between simulations in either surface stress curl or surface buoyancy fluxes. Moreover, the surface stress curl (Figure 8b) is weakest for the 0.1° simulation and there are no appreciable differences in the seasonal cycle of surface buoyancy fluxes (Figure 8c).

There are spatial differences in the amplitude of seasonal variability. The summer/winter anomalies with respect to the mean for the barotropic streamfunction in Figure 9a and c show that the largest seasonal variations are located in two separate regions around 30°W and 30°E respectively. The first region is located adjacent to a region of significant buoyancy gain during summer and the latter is located beneath the regional low pressure system (Figures 9b and d) which deepens and expands during the winter months and is shallower during summer, modifying the local wind pattern. The gyre boundary,

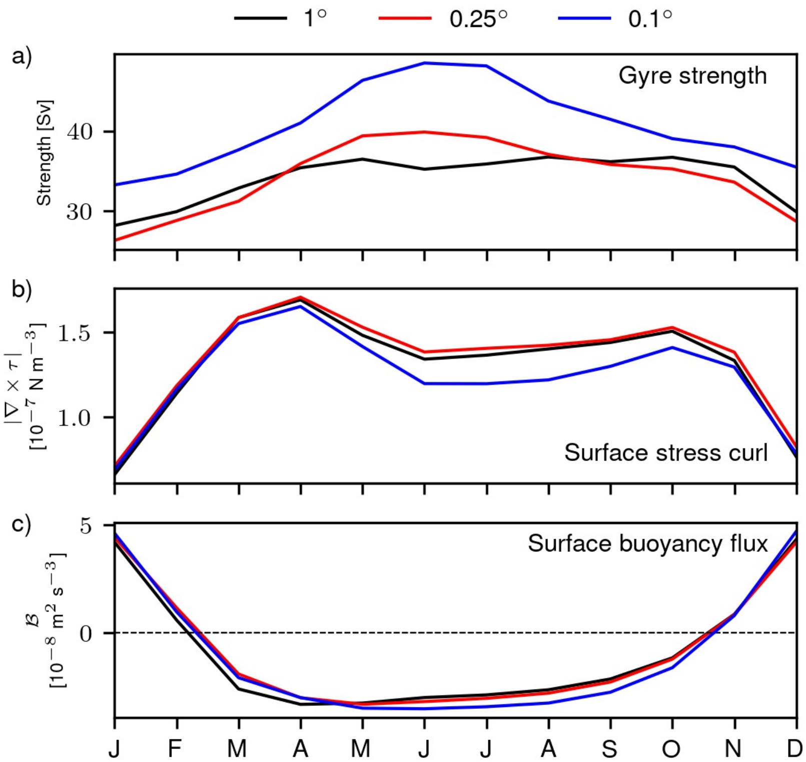

Figure 8. Annual cycles of (a) gyre strength (Sv), (b) surface stress curl ($10^{-7}Nm^{-3}$) averaged over the region bounded by the solid orange box in Figure 1 and (c) surface buoyancy flux ($10^{-8}m^2s^{-3}$) averaged at depths shallower than 1000 m.

Table 2. Correlation coefficients between gyre strength and surface stress curl, buoyancy flux, SAM index and EAS index for seasonal and interannual time scales. Bold values indicate significant correlations with $p < 0.05$.

Seasonal			
		$\|\nabla \times \tau\|$	$\mathcal{B}$
Gyre strength	1°	**0.82**	**-0.81**
	0.25°	**0.71**	**-0.89**
	0.1°	0.38	**-0.83**

Interannual					
		$\|\nabla \times \tau\|$	$\mathcal{B}$	SAM	EAS
Gyre strength	1°	0.04	-0.11	-0.36	0.26
	0.25°	0.21	-0.32	-0.24	0.34
	0.1°	0.21	-0.29	-0.19	**0.51**

defined by the 12 Sv contour, shows a general expansion during winter in all directions, with a particularly large excursion towards the east.

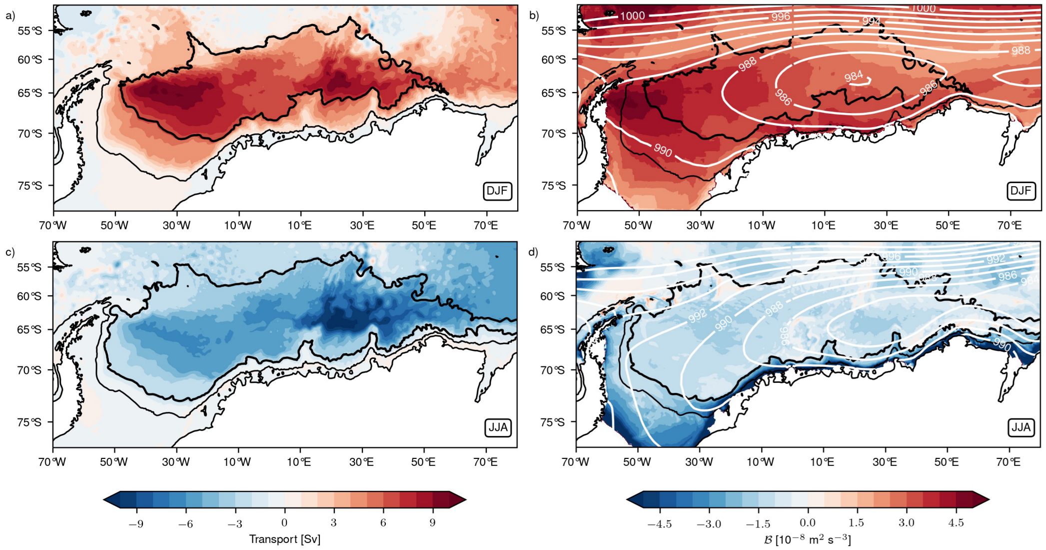

Figure 9. (a) Summer and (c) winter anomalies of ψ and (b) summer and (d) winter climatological fields of net surface buoyancy fluxes with and sea level pressure (white contours) for the 0.1° resolution case. Thin black contour indicates the 1000m isobath and thick black contour the Weddell Gyre's boundary in the corresponding season.

5 Weddell Gyre Interannual Variability

In order to explore the interannual variability of the Weddell Gyre and its connection to regional and large scale climate, we analyse the full 61-year period time series of anomalies with respect to the seasonal cycle of buoyancy fluxes, surface stress curl, gyre strength and the SAM and EAS index calculated as described in Section 2. These time series are shown in Figure 10. Gyre strength displays significant interannual variability that becomes greater in magnitude with resolution, with standard deviations of 4.5, 5 and 6 Sv for the 1°, 0.25° and 0.1° configurations respectively. There are some years which show an intensification of around 10 Sv, which is between a third and a quarter of the gyre's mean strength depending on the resolution. The strengths of the three configurations are mostly in phase and significantly correlated with each other, indicating the predominance of external forcing in driving the gyre's interannual variability. Similar to what was observed for the seasonal cycles, there is a clear influence of model resolution in setting the magnitude of gyre strength and the increase in magnitude from the 1° and 0.25° simulations to the 0.1° is not related to differences between resolutions in surface stress curl or buoyancy fluxes. Correlations between gyre strength and the other time series in Figure 10 are shown in Table 2. From the climate metrics considered here, only EAS shows a significant correlation with gyre strength for the 0.1° resolution configuration.

Next we identify strong events and weak events of gyre strength in the 0.1° resolution simulation, highlighted in red and blue shading respectively in Figure 10. There is no periodicity or seasonality in the occurrence of these events, i.e. extreme strong and weak events do not have a preference for particular months or seasons. Figure 11a shows the composites of strong events minus the composites of weak events for the barotropic streamfunction and sea level pressure. Since the cyclonic circulation of the Weddell Gyre is represented by $\psi < 0$ (Figure 6), negative anomalies indicate an intensified circulation. Sea level pressure shows a deepening and displacement to the west of a low pressure system that deepens the trough in the southern portion of the gyre, thus intensi-

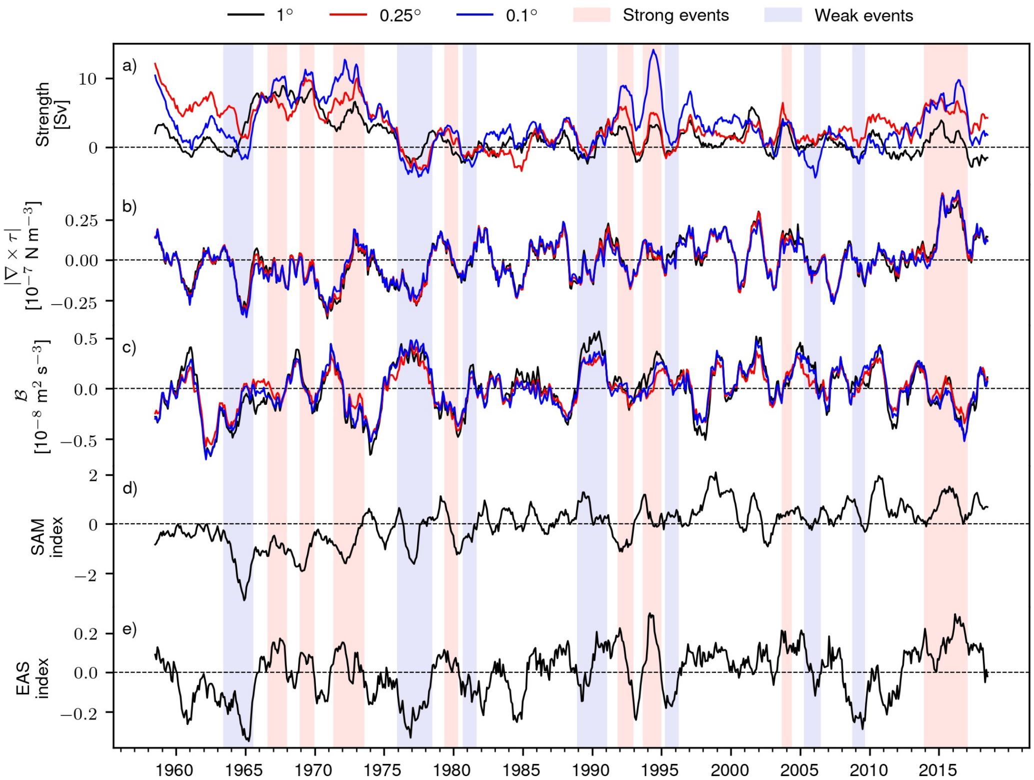

Figure 10. Time series of monthly anomalies with respect to the long term seasonal cycle of (a) gyre strength (Sv), (b) surface buoyancy flux ($10^{-8}m^2s^{-3}$), (c) surface stress curl ($10^{-7}Nm^{-3}$), (d) SAM index and (e) EAS index for the 1°, 0.25° and 0.1° resolutions. A 12-month running filter was applied to all time series. Red and blue shading indicate strong and weak events respectively for the 0.1° simulation.

fying the local easterly winds. The composites of surface buoyancy flux, Figure 11b show that during strong years, the southwestern region of the gyre experiences buoyancy loss in a region where buoyancy fluxes are significantly correlated with gyre strength, as marked by the hatching. These changes in buoyancy fluxes are consistent with the composite for sea ice concentration in Figure 11d: i.e., a stronger circulation advects sea ice from the southwestern region, decreasing its concentration during strong years, exposing the ocean's surface to the atmosphere, thus enabling a larger buoyancy loss. The ice is advected to the north and then to the east, generating an increase of almost 10% in sea ice concentration at the northern rim of the gyre. Another region where strength impacts sea ice concentration is the eastern boundary, where we see a decrease in concentration during stronger years consistent with a stronger warm inflow. Stronger years also display warmer subsurface temperature maxima along the southern region of the gyre that translate into a warmer continental shelf, Figure 11c. At around 30°E there are significant correlations between the subsurface temperature maximum, indicating synchronous changes in gyre strength and the characteristics of the warm inflow.

6 Discussion and Summary

In this study we have used a coupled ocean-sea ice model at three different horizontal resolutions (1°, 0.25° and 0.1°) to diagnose the circulation of the Weddell Gyre

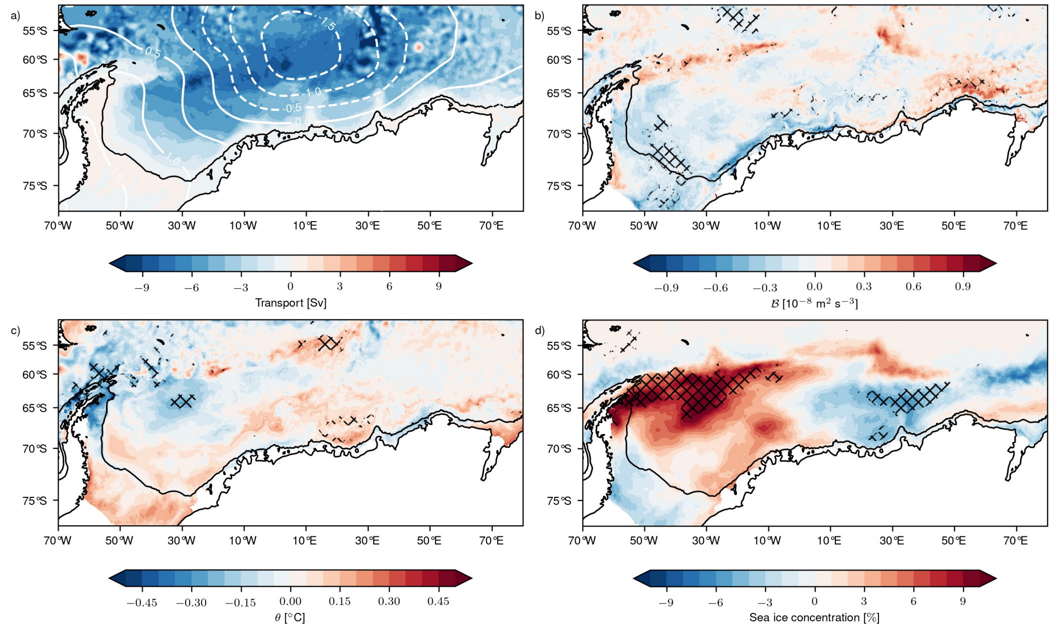

Figure 11. Strong minus weak Weddell Gyre composites of monthly anomalies for the events highlighted in Figure 10. Composites of (a) barotropic streamfunction (Sv) with sea level pressure contours overlaid (HPa), (b) surface buoyancy flux ($10^{-8}Nm^{-3}$), (c) subsurface temperature maximum (°C) and (d) sea ice concentration (%) for the 0.1° simulation. Hatching indicates significant correlations ($p < 0.1$) between gyre strength time series and the corresponding field..

and its connection to possible forcing mechanisms, namely surface stress forcing (including the contributions of wind and sea ice) and surface buoyancy fluxes. The inclusion of sea ice and the additional consideration of surface buoyancy fluxes expands on past studies that solely consider wind forcing due to the lack of appropriate observations. We evaluate the model against available satellite observations and hydrographic data and find a distinct improvement with resolution, particularly in the representation of the characteristics of regional water masses, which we suggest is a direct consequence of the ability of the 0.1° configuration to resolve instabilities along the eastern boundary of the gyre. The model displays significant seasonal and interannual variability in gyre strength, the magnitude of which increases with resolution. We find that extreme events of gyre circulation are climatically distinct, with significant differences in sea ice concentration and water mass characteristics during strong and weak phases of Weddell Gyre flow.

Our analysis indicates that most of the variability in gyre strength is concentrated in the seasonal cycle, which explains between 35% and 45% of the variance depending on the model's horizontal resolution. This seasonal cycle consists of a winter intensification and a summer weakening, in agreement with past studies (Dellnitz et al., 2009; Beckmann et al., 1999), that increases in magnitude with resolution. Consequently, estimates obtained from summer-biased observations will underestimate the gyre's transport, stressing the importance of sustained, continuous observations in the Weddell region. We further find that the seasonal changes in the barotropic circulation are not spatially uniform, but are concentrated in an eastern and a western region at approximately 30°W and 30°E respectively. Surface stress curl displays a semi-annual seasonal cycle peaking in April and October, highlighting the importance of sea ice in modulating the transfer of momentum from the atmosphere to the ocean, as emphasized by A. Naveira Garabato et al. (2019). Sea ice is also relevant for the seasonal cycle of surface buoyancy fluxes, where the ocean gains buoyancy during summer due to sea ice melt and loses surface buoyancy during winter due to sea ice formation.

The gyre also displays significant variability on interannual timescales, with gyre strength in phase across the three model resolutions, indicating the primacy of atmospheric forcing in driving the gyre's variability. However, the variations in gyre strength become more pronounced with resolution, the consequences of which we explored by means of composites of strong and weak events on interannual timescales using the 0.1° configuration. The composites show that the gyre circulation has an impact on relevant processes within the region: a stronger gyre coincides with a warmer inflow at the eastern boundary that warms up the continental shelf and induces large changes in sea ice concentration by advection towards the northern rim. Anomalous gyre events over interannual timescales are associated with a deepening and expansion to the west of the regional low pressure system that deepens the trough and accelerates the coastal easterlies. This acceleration of the easterlies increases the onshore Ekman transport, raising the slope in sea level and accelerating the southern limb of the Weddell Gyre, a mechanism supported by the significant correlation between gyre strength and the easterlies at 0.1° model resolution.

For the purpose of this study we have considered two possible forcing mechanisms for the Weddell Gyre's variability: namely surface stress curl, traditionally supposed to drive the circulation in the depth-integrated circulation of the ocean via a linear vorticity relationship with the ocean's meridional transport (Munk, 1950; Sverdrup, 1947), and buoyancy fluxes, which some studies suggest can maintain a gyre-like circulation (Hogg & Gayen, 2020; Wang & Meredith, 2008) and even drive a mean ACC (Howard et al., 2015; Hogg, 2010). The weak stratification that characterizes the region, together with intense surface buoyancy fluxes, drive an overturning circulation (Jullion et al., 2014; A. C. Naveira Garabato et al., 2016) that could affect the gyre's circulation via changes in its stratification. The coupling between ocean and sea ice in the model used for this study does not allow us to consider the independent contributions from buoyancy fluxes and surface stress. For example, on seasonal timescales, the lower resolution model's gyre strength is correlated with both surface stress curl and surface buoyancy fluxes, yet on interannual timescales neither show a clear correlation. Thus, the simulations presented here cannot ascertain which factors, or non-linear interactions between them, are more relevant in driving the gyre's variability. We conclude that more targeted numerical experiments are needed to address this question and to separate out stress from buoyancy forcing.

The importance of model resolution in the region is emphasized by its evaluation against hydrographic observations. Because of the Weddell Gyre's open configuration at its eastern boundary, the properties of the water masses in the region are highly influenced by the characteristics of the inflow (Kerr et al., 2018; Jullion et al., 2014; Couldrey et al., 2013). Two possible pathways have been suggested for this inflow: an eddy-driven path in the northeastern gyre boundary and an advective path further south towards the Antarctic continent (Ryan et al., 2016; Cisewski et al., 2011; Leach et al., 2011; Gouretski & Danilov, 1993). The eddy-driven inflow can be identified by a subsurface temperature maxima that is only reproduced by the 0.1° configuration, indicating that finer scale resolution processes are important for the exchange of waters between the gyre and its surroundings. The characteristics of this warm inflow are likely responsible for the improvement with resolution of the temperature-salinity structure of the Weddell Gyre, potentially also affecting the characteristics of bottom waters in the model.

The variability of the Weddell Gyre has the potential to impact regional processes of relevance to global climate, but there is still not a complete understanding of the gyre's driving mechanisms and timescales of interaction. We have considered surface stress and buoyancy fluxes as possible drivers of variability, but in a coupled ocean-sea ice model their intertwined nature does not allow us to consider them as independent mechanisms. It has also been suggested that the northern and southern limbs of the gyre vary independently, forced by the westerlies and easterlies respectively, with the difference balanced by inflows/outflows enabled by the gyre's open boundaries (Fahrbach et al., 2011). Our definition of gyre strength using the barotropic streamfunction is not intended to capture this independent variation. Remote forcing via the propagation of anomalies along the Antarctic continent could also affect the Weddell Gyre's circulation, but assessing this hypothesis is beyond the scope of this study. The 0.1° resolution model has the ability to reproduce observed key features of this polar region and provides a 61-year long data set that can prove useful for expanding our current knowledge of the Weddell Gyre.

Acknowledgments

This work was supported by the Australian Research Council, including the ARC Centre of Excellence for Climate Extremes, and the Climate Change Research Centre of the University of New South Wales. Numerical simulations and their analysis were conducted at the NCI National Facility systems at the Australian National University through the National Computational Merit Allocation Scheme. We thank the COSIMA consortium for its continuous support and constructive discussions and Thomas W.K. Armitage for generously providing the satellite observations used to evaluate our numerical model. The model output for the simulations presented in this paper are stored in the COSIMA data collection, available from `http://dx.doi.org/10.4225/41/5a2dc8543105a`. The analytical scripts used to generate the figures are available at `https://github.com/julia-neme`

References

Armitage, T. W., Kwok, R., Thompson, A. F., & Cunningham, G. (2018). Dynamic topography and sea level anomalies of the southern ocean: Variability and teleconnections. *Journal of Geophysical Research: Oceans*, *123*(1), 613–630.

Beckmann, A., Hellmer, H. H., & Timmermann, R. (1999). A numerical model of the weddell sea: Large-scale circulation and water mass distribution. *Journal of Geophysical Research: Oceans*, *104*(C10), 23375–23391.

Behrendt, A., Fahrbach, E., Hoppema, M., Rohardt, G., Boebel, O., Klatt, O., … Witte, H. (2011). Variations of winter water properties and sea ice along the greenwich meridian on decadal time scales. *Deep Sea Research Part II: Topical Studies in Oceanography*, *58*(25-26), 2524–2532.

Cisewski, B., Strass, V. H., & Leach, H. (2011). Circulation and transport of water masses in the lazarev sea, antarctica, during summer and winter 2006. *Deep Sea Research Part I: Oceanographic Research Papers*, *58*(2), 186–199.

Couldrey, M. P., Jullion, L., Naveira Garabato, A. C., Rye, C., Herráiz-Borreguero, L., Brown, P. J., … Speer, K. L. (2013). Remotely induced warming of antarctic bottom water in the eastern weddell gyre. *Geophysical Research Letters*, *40*(11), 2755–2760.

Deacon, G. (1979). The weddell gyre. *Deep Sea Research Part A. Oceanographic Research Papers*, *26*(9), 981–995.

Dellnitz, M., Froyland, G., Horenkamp, C., Padberg-Gehle, K., & Sen Gupta, A. (2009). Seasonal variability of the subpolar gyres in the southern ocean: a numerical investigation based on transfer operators. *Nonlinear Processes in Geophysics*, *16*(6), 655–663.

Fahrbach, E., Hoppema, M., Rohardt, G., Boebel, O., Klatt, O., & Wisotzki, A. (2011). Warming of deep and abyssal water masses along the greenwich meridian on decadal time scales: The weddell gyre as a heat buffer. *Deep Sea Research Part II: Topical Studies in Oceanography*, *58*(25-26), 2509–2523.

Fahrbach, E., Hoppema, M., Rohardt, G., Schröder, M., & Wisotzki, A. (2004). Decadal-scale variations of water mass properties in the deep weddell sea. *Ocean Dynamics*, *54*(1), 77–91.

Fahrbach, E., Knoche, M., & Rohardt, G. (1991). An estimate of water mass transformation in the southern weddell sea. *Marine Chemistry*, *35*(1-4), 25–44.

Fecher, T., Pail, R., Gruber, T., Consortium, G., et al. (2017). Goco05c: a new combined gravity field model based on full normal equations and regionally varying weighting. *Surveys in geophysics*, *38*(3), 571–590.

Gordon, A., Martinson, D., & Taylor, H. (1981). The wind-driven circulation in the weddell-enderby basin. *Deep Sea Research Part A. Oceanographic Research Papers*, *28*(2), 151–163.

Gouretski, V. V., & Danilov, A. I. (1993). Weddell gyre: structure of the eastern boundary. *Deep Sea Research Part I: Oceanographic Research Papers*, *40*(3), 561–582.

Hogg, A. M. (2010). An antarctic circumpolar current driven by surface buoyancy forcing. *Geophysical Research Letters*, *37*(23).

Hogg, A. M., & Gayen, B. (2020). Ocean gyres driven by surface buoyancy forcing. *Geophysical Research Letters*, *47*(16), e2020GL088539.

Howard, E., McC. Hogg, A., Waterman, S., & Marshall, D. P. (2015). The injection of zonal momentum by buoyancy forcing in a southern ocean model. *Journal of Physical Oceanography*, *45*(1), 259–271.

Jullion, L., Garabato, A. C. N., Bacon, S., Meredith, M. P., Brown, P. J., Torres-Valdés, S., … others (2014). The contribution of the weddell gyre to the lower limb of the global overturning circulation. *Journal of Geophysical Research: Oceans*, *119*(6), 3357–3377.

Jullion, L., Jones, S., Naveira Garabato, A., & Meredith, M. P. (2010). Wind-controlled export of antarctic bottom water from the weddell sea. *Geophysical Research Letters*, *37*(9).

Kerr, R., Dotto, T. S., Mata, M. M., & Hellmer, H. H. (2018). Three decades of deep water mass investigation in the weddell sea (1984–2014): temporal variability and changes. *Deep Sea Research Part II: Topical Studies in Oceanography*, *149*, 70–83.

Kiss, A. E., Hogg, A. M., Hannah, N., Boeira Dias, F., Brassington, G. B., Chamberlain, M. A., … others (2020). Access-om2 v1. 0: a global ocean-sea ice model at three resolutions. *Geoscientific Model Development*, *13*(2), 401–442.

Klatt, O., Fahrbach, E., Hoppema, M., & Rohardt, G. (2005). The transport of the weddell gyre across the prime meridian. *Deep Sea Research Part II: Topical Studies in Oceanography*, *52*(3-4), 513–528.

Leach, H., Strass, V., & Cisewski, B. (2011). Modification by lateral mixing of the warm deep water entering the weddell sea in the maud rise region. *Ocean Dynamics*, *61*(1), 51–68.

Locarnini, M., Mishonov, A., Baranova, O., Boyer, T., Zweng, M., Garcia, H., … others (2018). World ocean atlas 2018, volume 1: Temperature.

Locarnini, R. A., Whitworth, T., & Nowlin, W. D. (1993). The importance of the scotia sea on the outflow of weddell sea deep water. *Journal of Marine Research*, *51*(1), 135–153.

Marshall, G. J. (2003). Trends in the southern annular mode from observations and reanalyses. *Journal of Climate*, *16*(24), 4134–4143.

Martinson, D. G., & Iannuzzi, R. A. (2003). Spatial/temporal patterns in weddell gyre characteristics and their relationship to global climate. *Journal of Geophysical Research: Oceans*, *108*(C4).

Mathiot, P., Goosse, H., Fichefet, T., Barnier, B., & Gallée, H. (2011). Modelling the seasonal variability of the antarctic slope current. *Ocean Science*, *7*(4), 455–470.

Mazloff, M. R., Heimbach, P., & Wunsch, C. (2010). An eddy-permitting southern ocean state estimate. *Journal of Physical Oceanography*, *40*(5), 880–899.

Meredith, M. P. (2013). Replenishing the abyss. *Nature Geoscience*, *6*(3), 166–167.

Meredith, M. P., Garabato, A. C. N., Gordon, A. L., & Johnson, G. C. (2008). Evolution of the deep and bottom waters of the scotia sea, southern ocean, during 1995–2005. *Journal of Climate*, *21*(13), 3327–3343.

Meredith, M. P., Gordon, A. L., Naveira Garabato, A. C., Abrahamsen, E. P., Huber, B. A., Jullion, L., & Venables, H. J. (2011). Synchronous intensification and warming of antarctic bottom water outflow from the weddell gyre. *Geophysical Research Letters*, *38*(3).

Moorman, R., Morrison, A. K., & McC. Hogg, A. (2020). Thermal responses to antarctic ice shelf melt in an eddy-rich global ocean–sea ice model. *Journal of Climate*, *33*(15), 6599–6620.

Morrison, A., Hogg, A. M., England, M. H., & Spence, P. (2020). Warm circumpolar deep water transport toward antarctica driven by local dense water export in canyons. *Science Advances*, *6*(18), eaav2516.

Munk, W. H. (1950). On the wind-driven ocean circulation. *Journal of meteorology*, *7*(2), 80–93.

Naveira Garabato, A., Dotto, T., Hooley, J., Bacon, S., Tsamados, M., Ridout, A., ... others (2019). Phased response of the subpolar southern ocean to changes in circumpolar winds. *Geophysical Research Letters*, *46*(11), 6024–6033.

Naveira Garabato, A. C., Zika, J. D., Jullion, L., Brown, P. J., Holland, P. R., Meredith, M. P., & Bacon, S. (2016). The thermodynamic balance of the weddell gyre. *Geophysical Research Letters*, *43*(1), 317–325.

Orsi, A. H., Nowlin Jr, W. D., & Whitworth III, T. (1990). *On the circulation and stratification of the weddell gyre* (Unpublished master's thesis). Texas A&M University.

Park, Y.-H., & Gambéroni, L. (1995). Large-scale circulation and its variability in the south indian ocean from topex/poseidon altimetry. *Journal of Geophysical Research: Oceans*, *100*(C12), 24911–24929.

Reeve, K. A., Boebel, O., Kanzow, T., Strass, V. H., Rohardt, G., & Fahrbach, E. (2016). *Objective Mapping of Argo data in the Weddell Gyre: a gridded dataset of upper ocean water properties, link to data files in NetCDF format* [data set]. PANGAEA. Retrieved from `https://doi.org/10.1594/PANGAEA.842876` (Supplement to: Reeve, KA et al. (2016): A gridded data set of upper-ocean hydrographic properties in the Weddell Gyre obtained by objective mapping of Argo float measurements. Earth System Science Data, 8(1), 15-40, https://doi.org/10.5194/essd-8-15-2016) doi: 10.1594/PANGAEA.842876

Reeve, K. A., Boebel, O., Strass, V., Kanzow, T., & Gerdes, R. (2019). Horizontal circulation and volume transports in the weddell gyre derived from argo float data. *Progress in Oceanography*, *175*, 263–283.

Ryan, S., Schröder, M., Huhn, O., & Timmermann, R. (2016). On the warm inflow at the eastern boundary of the weddell gyre. *Deep Sea Research Part I: Oceanographic Research Papers*, *107*, 70–81.

Schröder, M., & Fahrbach, E. (1999). On the structure and the transport of the eastern weddell gyre. *Deep Sea Research Part II: Topical Studies in Oceanography*, *46*(1-2), 501–527.

Sverdrup, H. U. (1947). Wind-driven currents in a baroclinic ocean; with application to the equatorial currents of the eastern pacific. *Proceedings of the National Academy of Sciences of the United States of America*, *33*(11), 318.

Tsujino, H., Urakawa, S., Nakano, H., Small, R. J., Kim, W. M., Yeager, S. G., ... others (2018). Jra-55 based surface dataset for driving ocean–sea-ice models (jra55-do). *Ocean Modelling*, *130*, 79–139.

Wang, Z., & Meredith, M. (2008). Density-driven southern hemisphere subpolar gyres in coupled climate models. *Geophysical Research Letters*, *35*(14).

Zweng, M., Seidov, D., Boyer, T., Locarnini, M., Garcia, H., Mishonov, A., ... others (2019). World ocean atlas 2018, volume 2: Salinity.

Figure 1.

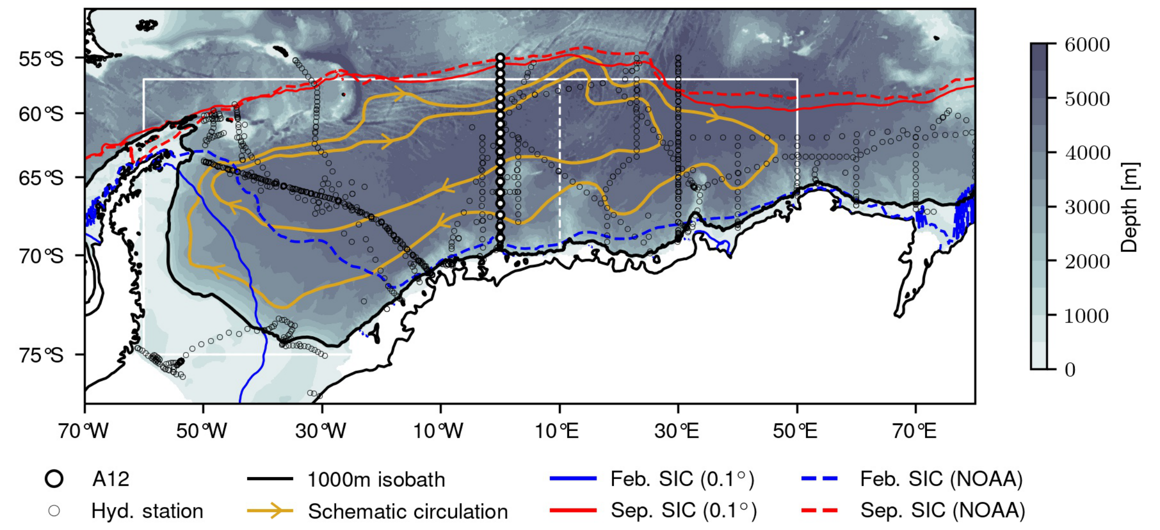
55°S
60°S
65°S
70°S
75°S
70°W
50°W
30°W
10°W
10°E
30°E
50°E
70°E
6000
5000
4000
3000
2000
1000
0
Depth [m]
A12
Hyd. station
1000m isobath
Schematic circulation
Feb. SIC (0.1°)
Sep. SIC (0.1°)
Feb. SIC (NOAA)
Sep. SIC (NOAA)

Figure 2.

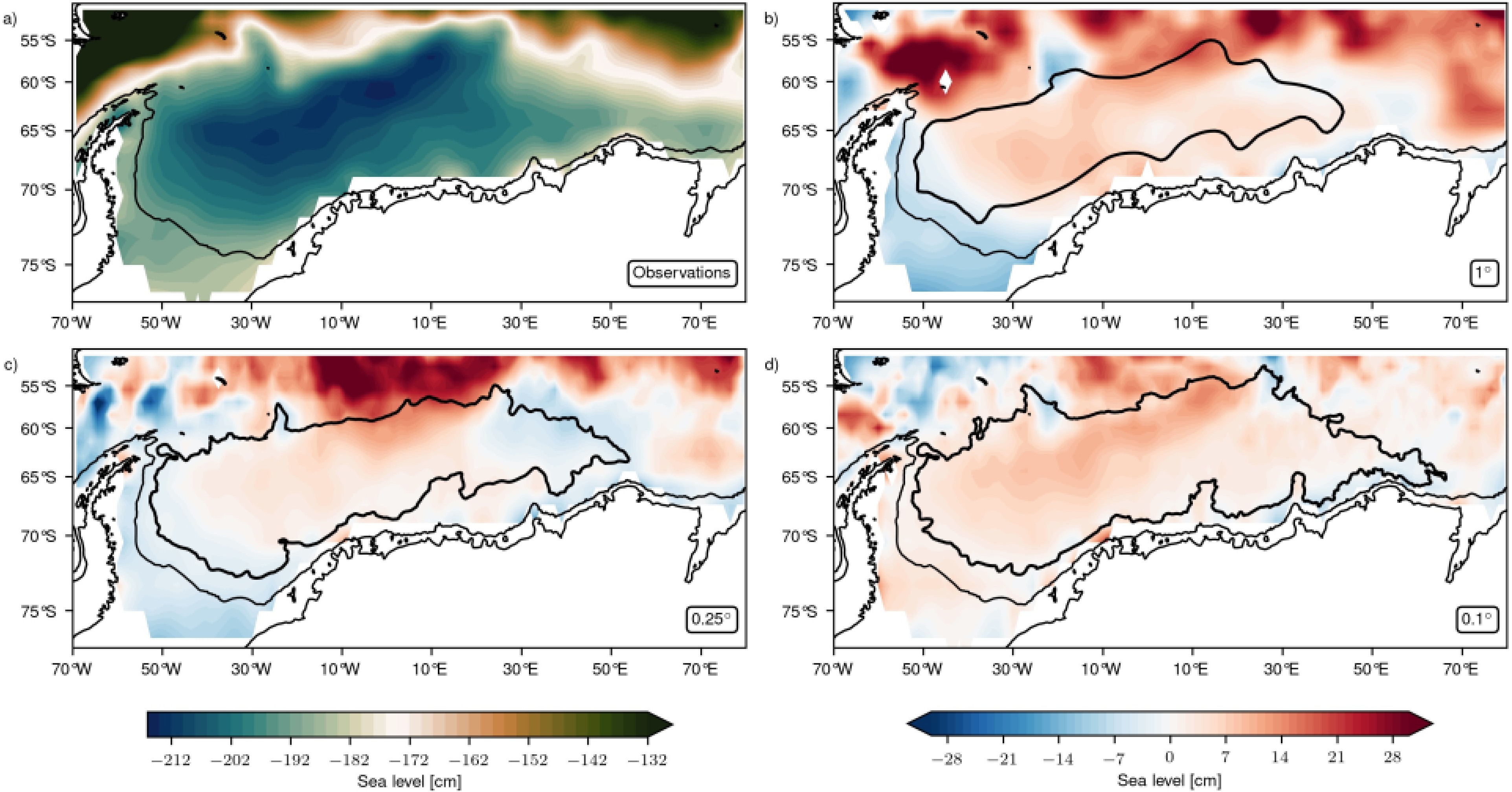
a)
b)
c)
d)
Observations
1°
0.25°
0.1°
55°S
60°S
65°S
70°S
75°S
70°W
50°W
30°W
10°W
10°E
30°E
50°E
70°E
−212
−202
−192
−182
−172
−162
−152
−142
−132
Sea level [cm]
−28
−21
−14
−7
0
7
14
21
28
Sea level [cm]

Figure 3.

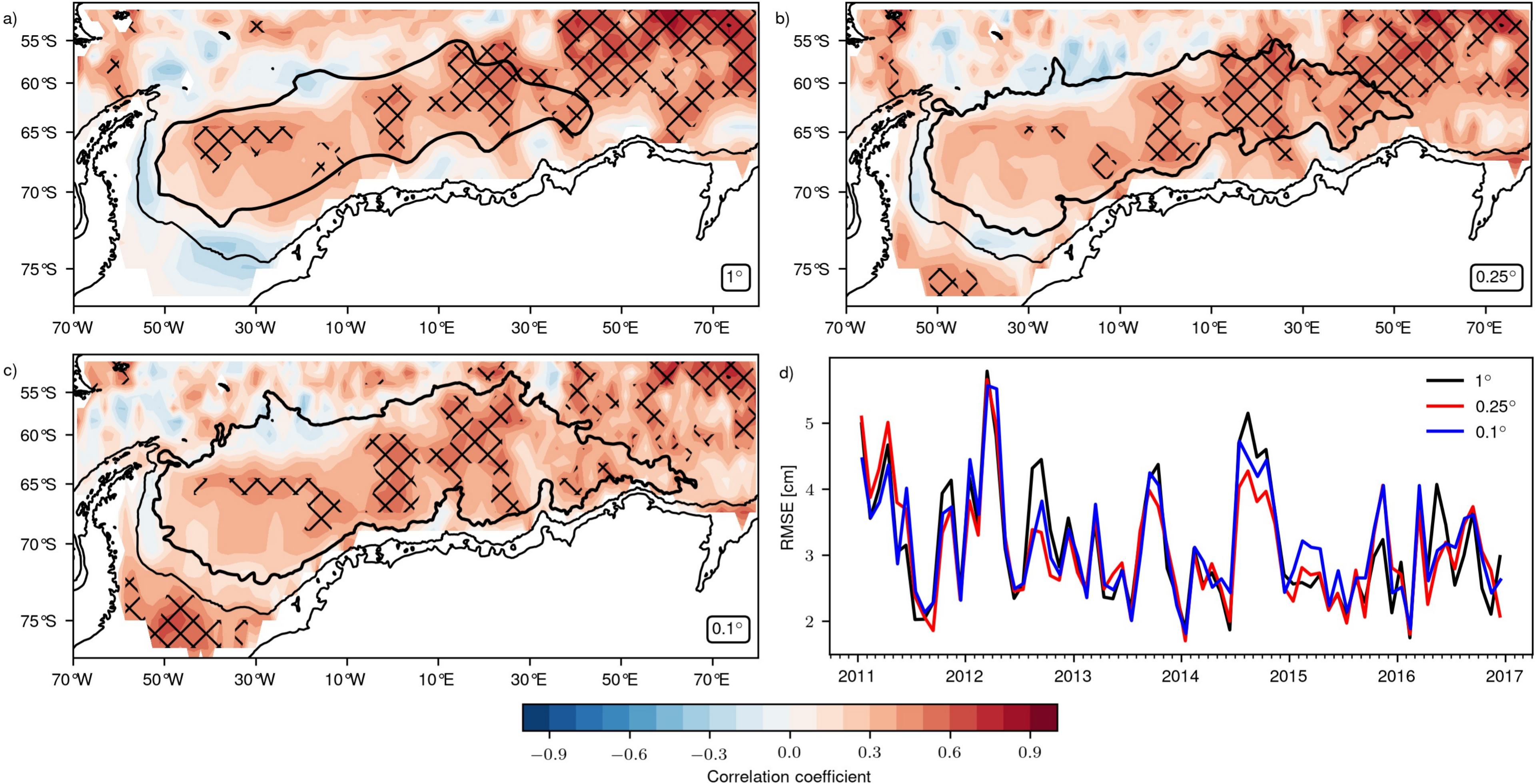
a)
55°S
60°S
65°S
70°S
75°S
70°W
50°W
30°W
10°W
10°E
30°E
50°E
70°E
1°
b)
0.25°
c)
0.1°
d)
RMSE [cm]
1°
0.25°
0.1°
2011
2012
2013
2014
2015
2016
2017
−0.9
−0.6
−0.3
0.0
0.3
0.6
0.9
Correlation coefficient

Figure 4.

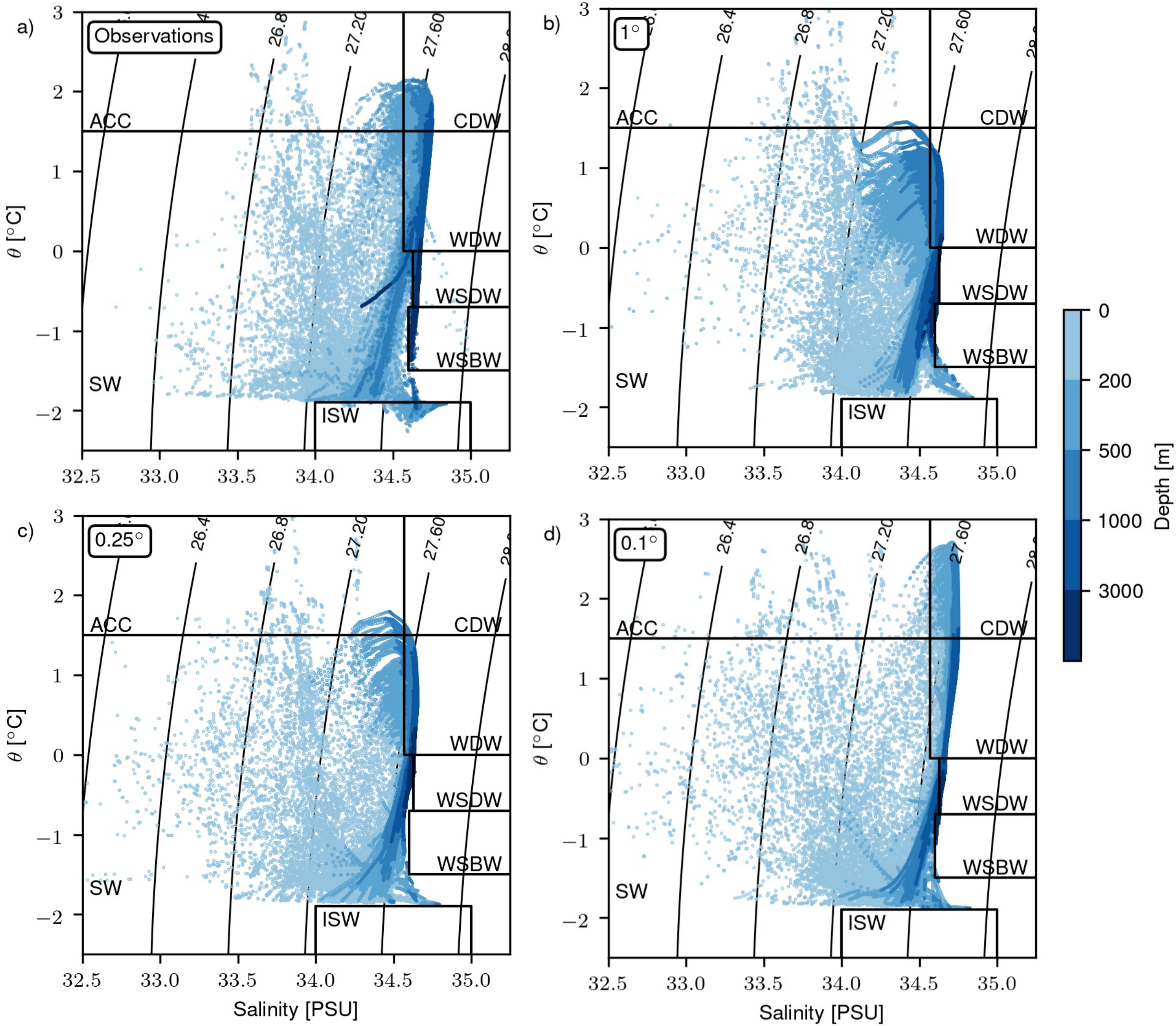

a)
Observations
b)
1°
c)
0.25°
d)
0.1°
ACC
CDW
WDW
WSDW
WSBW
SW
ISW
26.4
26.8
27.20
27.60
θ [°C]
Salinity [PSU]
Depth [m]
0
200
500
1000
3000

Figure 5.

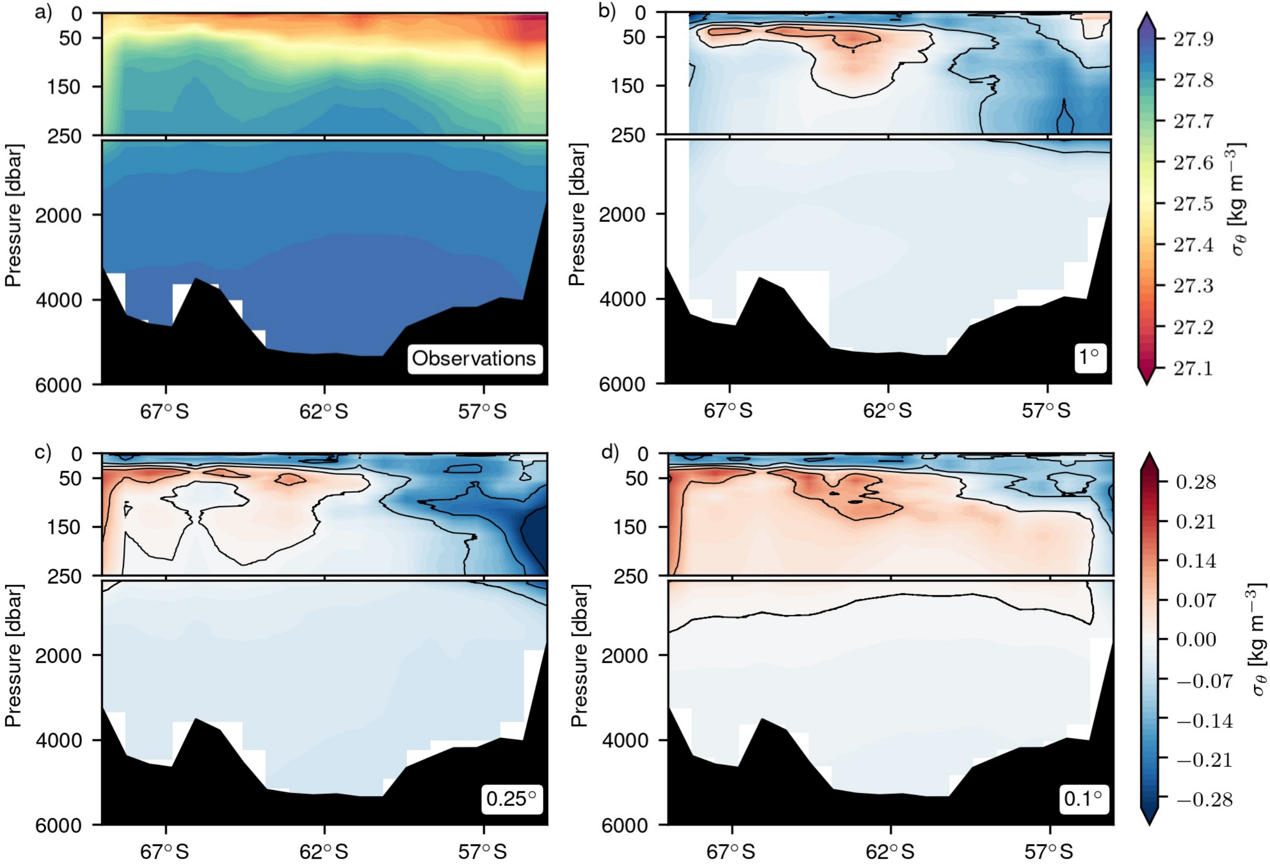

a)
b)
c)
d)
Pressure [dbar]
0
50
150
250
2000
4000
6000
67° S
62° S
57° S
Observations
1°
0.25°
0.1°
27.9
27.8
27.7
27.6
27.5
27.4
27.3
27.2
27.1
σθ [kg m−3]
0.28
0.21
0.14
0.07
0.00
−0.07
−0.14
−0.21
−0.28
σθ [kg m−3]

Figure 6.

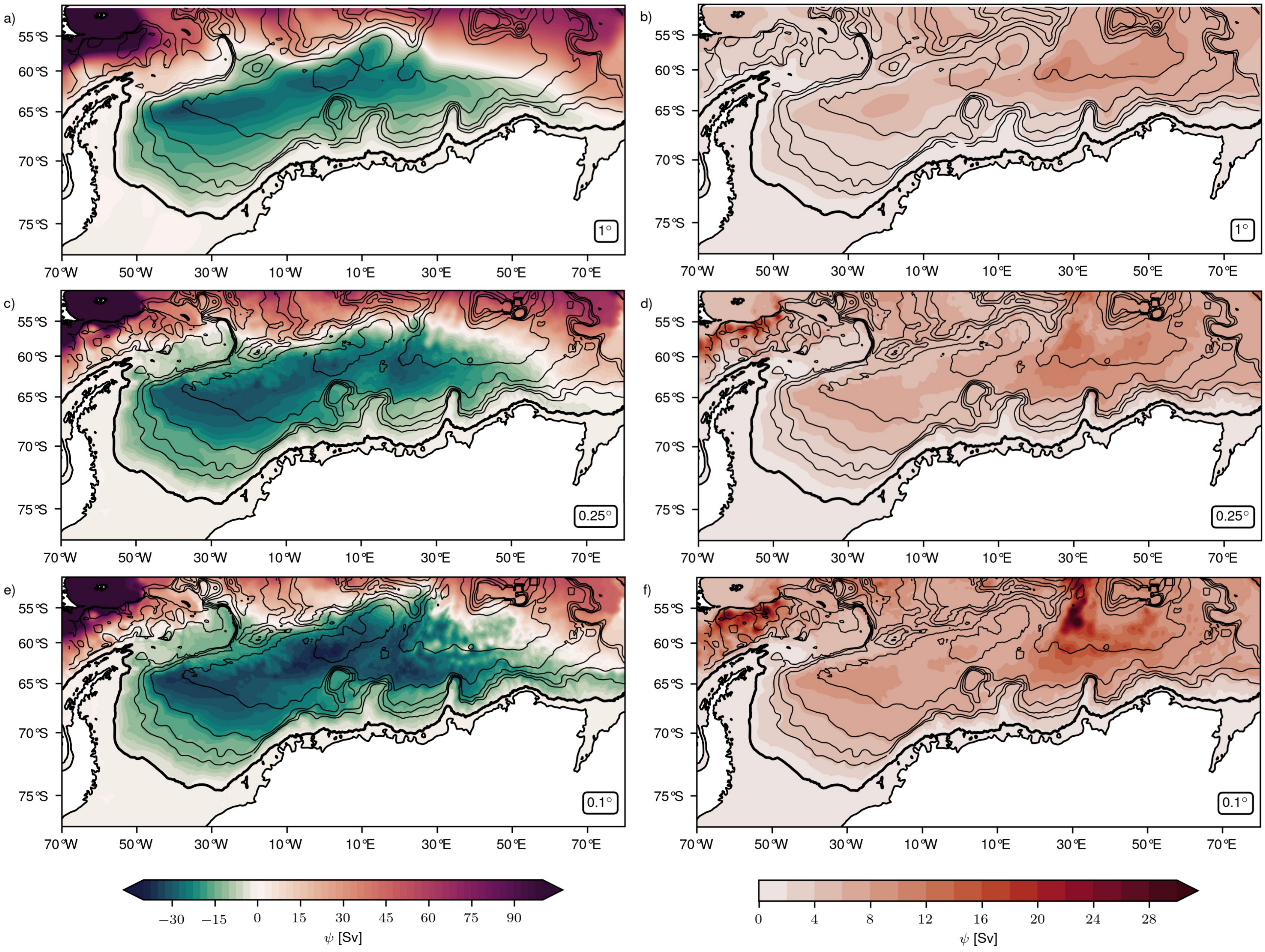

a)
b)
c)
d)
e)
f)
55°S
60°S
65°S
70°S
75°S
70°W
50°W
30°W
10°W
10°E
30°E
50°E
70°E
1°
0.25°
0.1°
−30
−15
0
15
30
45
60
75
90
ψ [Sv]
0
4
8
12
16
20
24
28
ψ [Sv]

Figure 7.

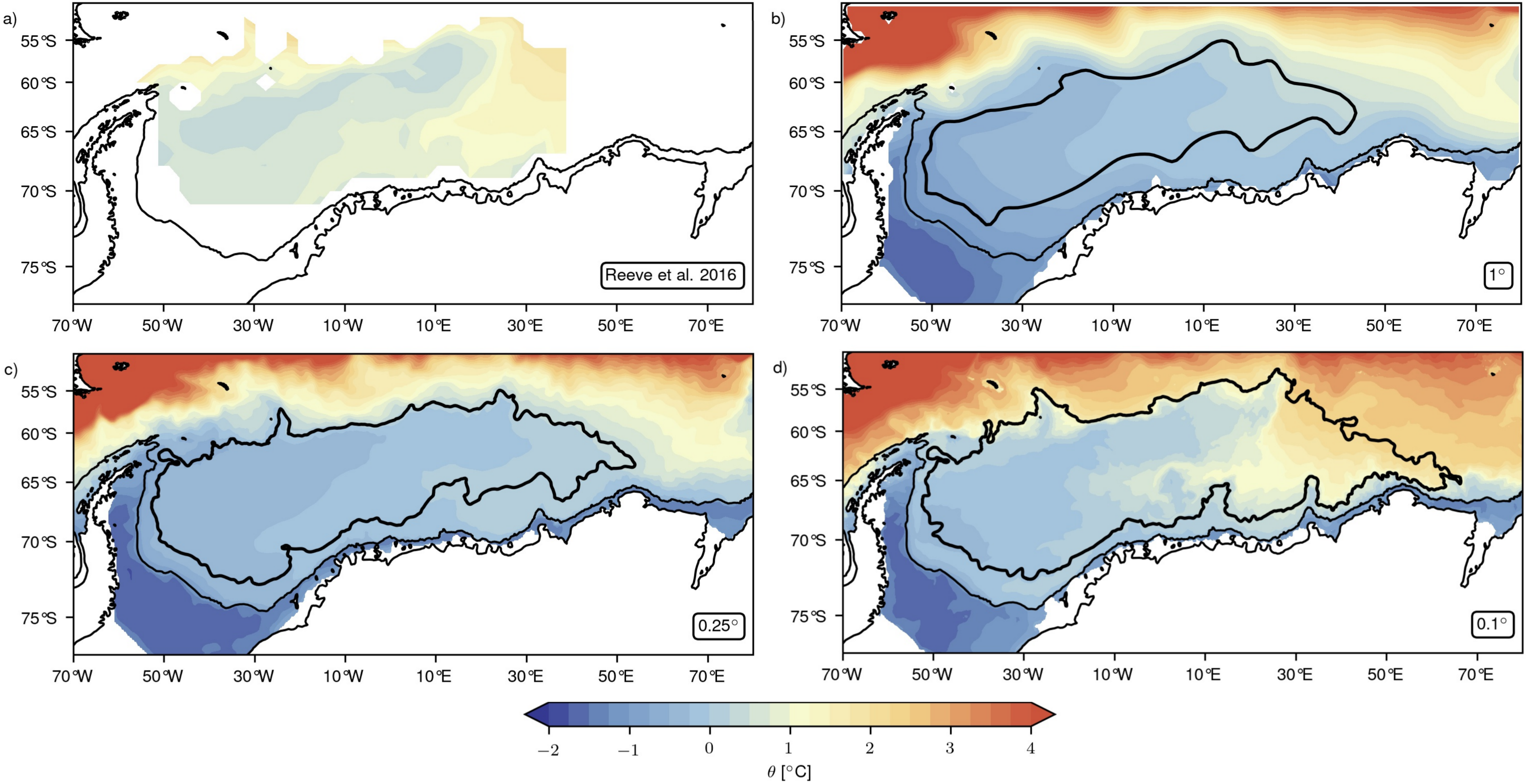

a)
b)
c)
d)
Reeve et al. 2016
1°
0.25°
0.1°
55°S
60°S
65°S
70°S
75°S
70°W
50°W
30°W
10°W
10°E
30°E
50°E
70°E
−2
−1
0
1
2
3
4
θ [°C]

Figure 8.

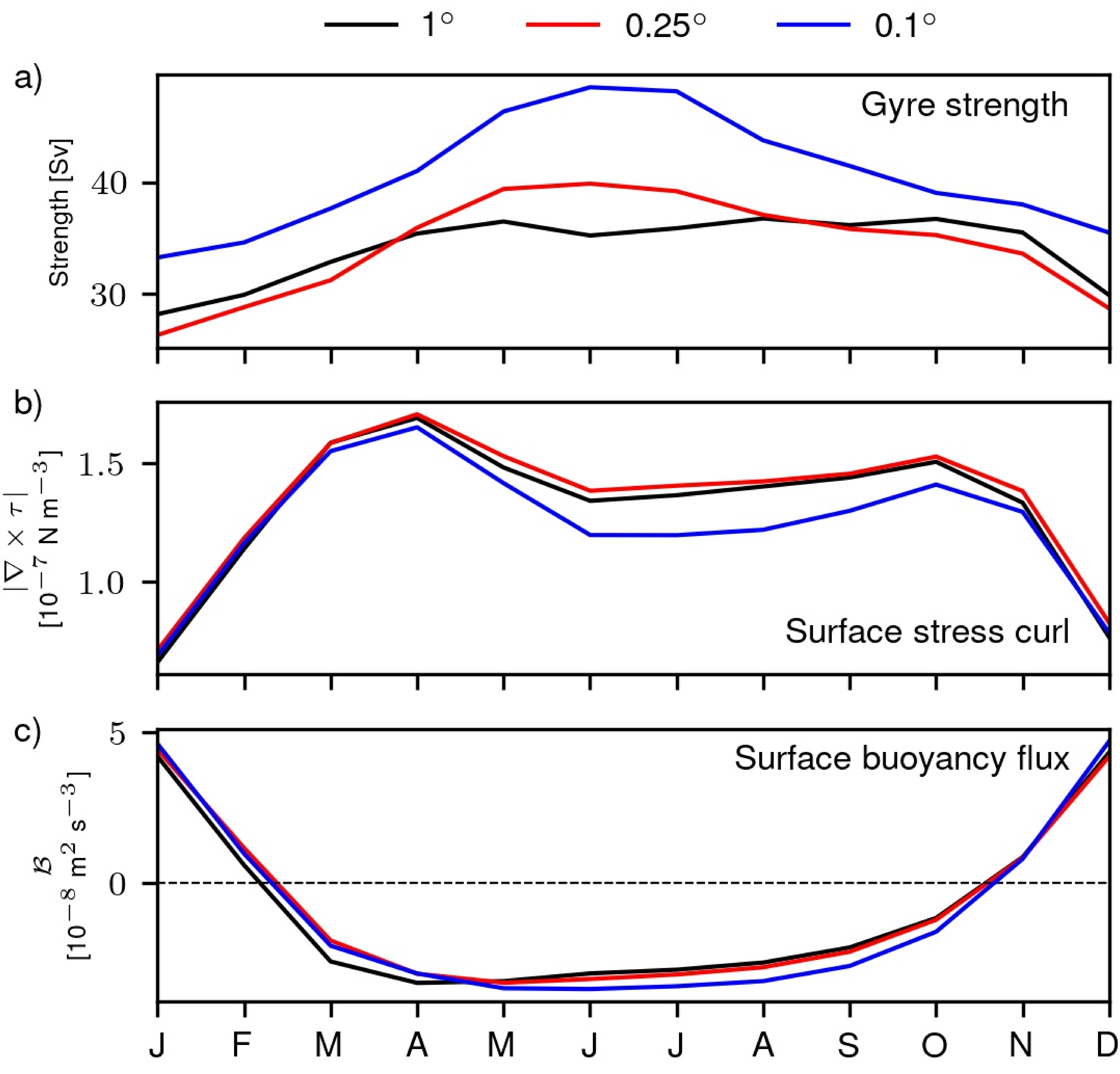
1°
0.25°
0.1°
a)
Gyre strength
Strength [Sv]
30
40
b)
Surface stress curl
$|\nabla \times \tau|$
[10^{-7} N m^{-3}]
1.0
1.5
c)
Surface buoyancy flux
$\mathcal{B}$
[10^{-8} m^2 s^{-3}]
0
5
J
F
M
A
M
J
J
A
S
O
N
D

Figure 9.

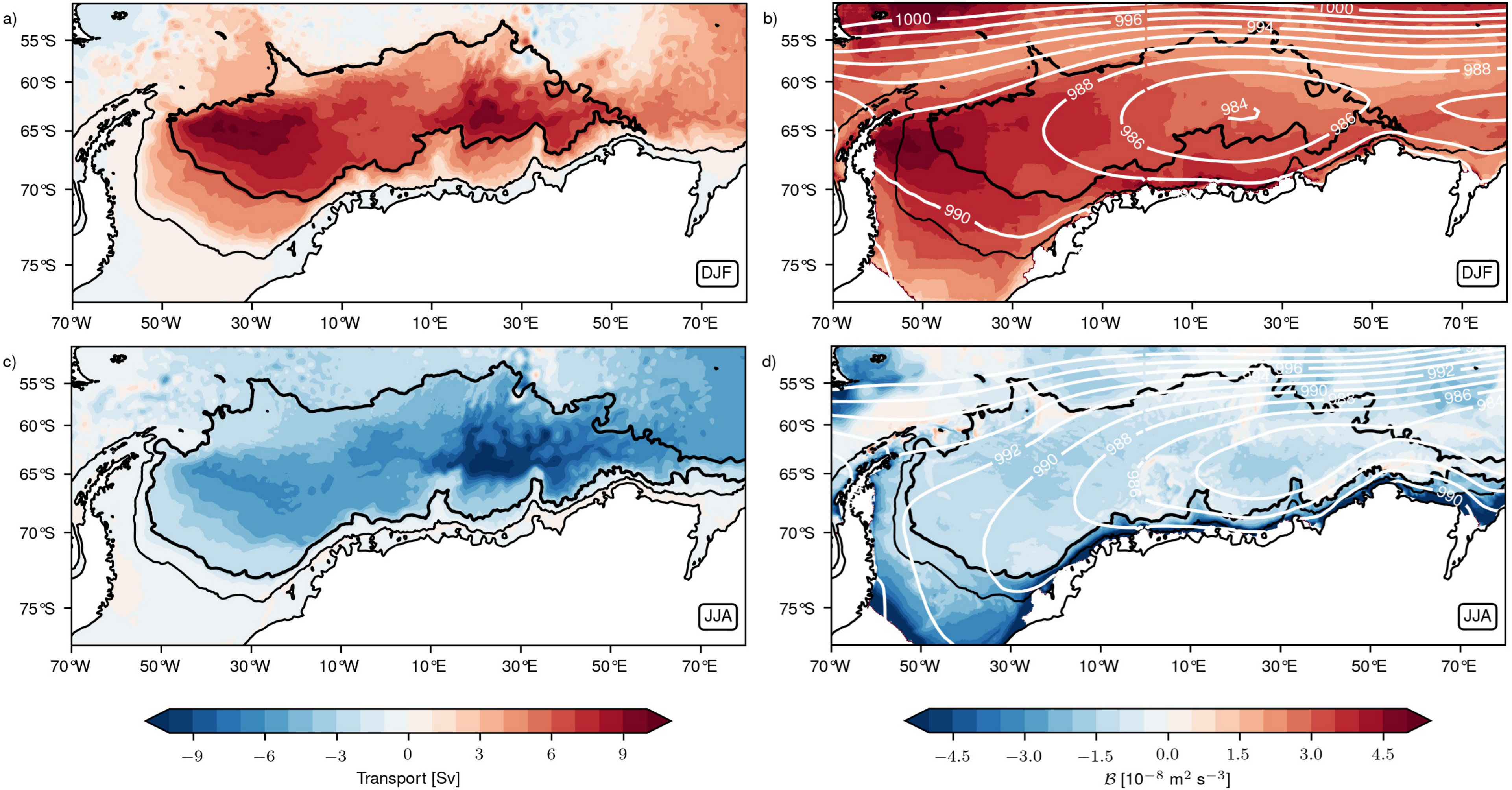

a)
b)
c)
d)
DJF
DJF
JJA
JJA
55°S
60°S
65°S
70°S
75°S
70°W
50°W
30°W
10°W
10°E
30°E
50°E
70°E
1000
996
994
988
984
986
990
992
−9
−6
−3
0
3
6
9
Transport [Sv]
−4.5
−3.0
−1.5
0.0
1.5
3.0
4.5
$\mathcal{B}$ [10^{-8} m^2 s^{-3}]

Figure 10.

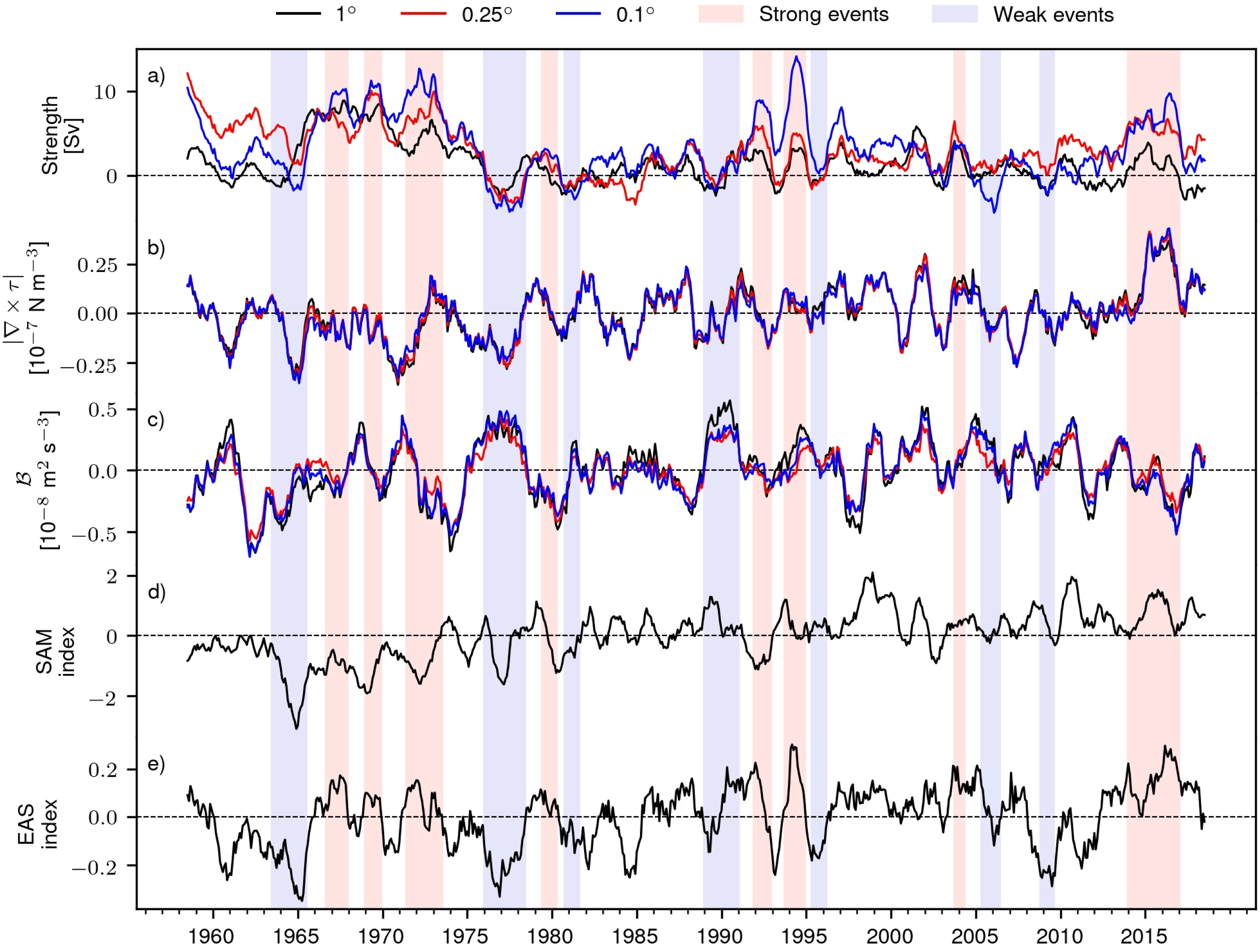
1°
0.25°
0.1°
Strong events
Weak events
a)
Strength [Sv]
10
0
b)
$|\nabla \times \tau|$ [10^{-7} N m^{-3}]
0.25
0.00
−0.25
c)
$\mathcal{B}$ [10^{-8} m^2 s^{-3}]
0.5
0.0
−0.5
d)
SAM index
2
0
−2
e)
EAS index
0.2
0.0
−0.2
1960
1965
1970
1975
1980
1985
1990
1995
2000
2005
2010
2015

Figure 11.

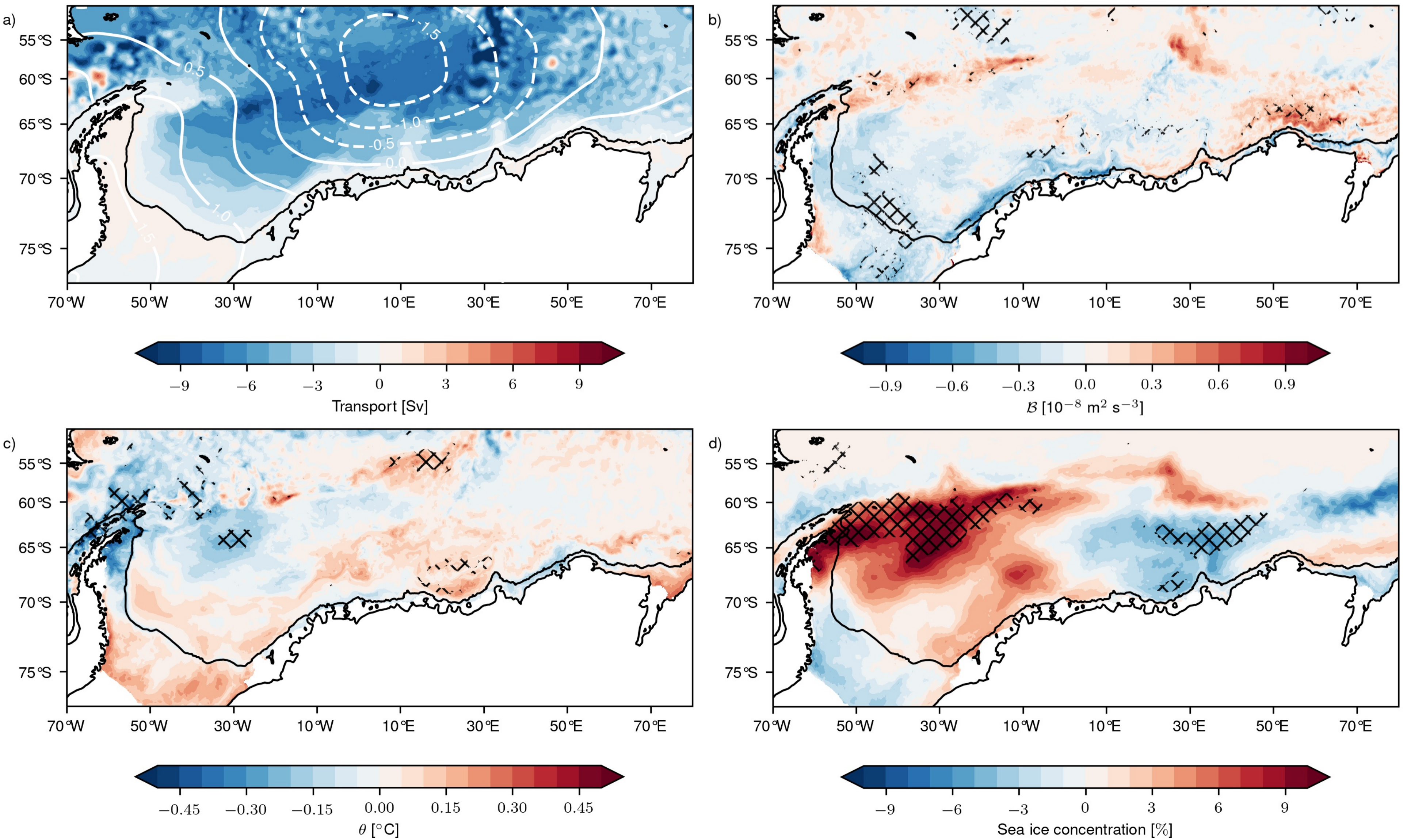
a)
b)
c)
d)
55°S
60°S
65°S
70°S
75°S
70°W
50°W
30°W
10°W
10°E
30°E
50°E
70°E
-1.5
-1.0
-0.5
0.0
0.5
1.0
1.5
−9
−6
−3
0
3
6
9
Transport [Sv]
−0.9
−0.6
−0.3
0.0
0.3
0.6
0.9
$\mathcal{B}$ [10^{-8} m^2 s^{-3}]
−0.45
−0.30
−0.15
0.00
0.15
0.30
0.45
θ [°C]
Sea ice concentration [%]